

2015-09-28

Molecular-Dynamics Simulations of Ice Growth from the Vapour Phase: Demonstration of Proof of Principle

Mohandesi, Ali

Mohandesi, A. (2015). Molecular-Dynamics Simulations of Ice Growth from the Vapour Phase: Demonstration of Proof of Principle (Master's thesis, University of Calgary, Calgary, Canada).

Retrieved from <https://prism.ucalgary.ca>. doi:10.11575/PRISM/26984

<http://hdl.handle.net/11023/2516>

Downloaded from PRISM Repository, University of Calgary

UNIVERSITY OF CALGARY

Molecular-Dynamics Simulations of Ice Growth from the Vapour Phase: Demonstration
of Proof of Principle

by

Ali Mohandesi

A THESIS

SUBMITTED TO THE FACULTY OF GRADUATE STUDIES IN PARTIAL
FULFILMENT OF THE REQUIREMENTS FOR THE DEGREE OF
MASTER OF SCIENCE

DEPARTMENT OF CHEMISTRY

CALGARY, ALBERTA

SEPTEMBER, 2015

© Ali Mohandesi 2015

Abstract

Ice plays important roles in atmospheric, environmental and biological phenomena and is found in various morphologies on Earth. Despite many investigations of ice growth from the vapor, the molecular-scale details of its mechanism have yet to be resolved. In this thesis, an MD simulation approach has been used to study ice growth from water vapor. Also, the dependence of the behavior of the quasi-liquid-layer (QLL) that forms on the ice surface on temperature, ice face and flux of particles in the gas was investigated. It was found that with increased temperature the thickness of the QLL also increases. In addition, the QLL on the basal face was thicker than on the prism face. Monitoring the QLL behavior on the basal face at 245 K during steady state growth demonstrated that increasing the flux of particles in the gas builds up an extra layer on the QLL.

Acknowledgements

First and foremost, I would like to express my sincerest gratitude to my supervisor Professor Peter Kusalik for his priceless support and guidance throughout my research and study. This work would not have been possible without his continuous support, suggestions, valuable discussions and patience.

I would like to convey my special thanks to Dr. Dmitri Rozmonov for his valuable guidance, suggestions, cooperation and time. His special expertise in this area is indispensable in making this research possible.

I am highly grateful to Dr. Edelsys Codorniu-Hernandez for her kindness and support and suggestions throughout my study.

Finally, I would like to express my love and thanks to my mother, Monir, and sister, Sanaz, whose support and patience have always been heartwarming and motivating. I would like to thank all of my friends in Calgary who alleviated the pain of being far from home.

to my mother, Monir, and sister, Sanaz,

and

to the memory of my father, Reza

Table of Contents

Abstract	ii
Acknowledgments	iii
Dedication	iv
Table of Contents	vi
List of Tables	vii
List of Figures	x
1 INTRODUCTION	1
1.1 Introduction	1
1.2 Water and ice properties	2
1.2.1 Water	2
1.2.2 Hexagonal ice Ih	5
1.2.3 The other phases of ice	6
1.2.4 Ice-vapor interface	8
1.3 Molecular dynamics	8
1.3.1 Constant temperature control	13
1.3.2 Constant pressure control	15
1.4 Water models	16
1.5 Literature review	24
1.5.1 Experimental studies	24
1.5.1.1 Ice growth from vapor	24
1.5.1.2 Quasi-liquid layer on the ice surface	27
1.5.2 Theoretical studies	28
2 STUDIES OF ICE GROWTH FROM WATER VAPOR	31
2.1 Methodology	31
2.1.1 Simulation details	31
2.1.2 System preparation	33
2.1.3 Temperature profile and surface detection	33
2.2 Results and Discussion	38
2.2.1 Summary of the Results of Simulations	38

2.2.2	Temperature dependence of the QLL thickness on different faces of ice	43
2.2.3	Comparison of the QLL thickness on the basal and prism faces of ice	45
2.2.4	Dependence of the QLL thickness on the flux of particles in gas . .	46
3	CONCLUSION AND FUTURE WORK	51
3.1	Conclusion	51
3.2	Future Work	52
	Bibliography	53
A	SUPPLEMENTARY FIGURES	62

List of Tables

1.1	Potential parameters of discussed water models. The type of water model corresponds to the schematic representations in Figure 1.7. d_{OH} is the distance between hydrogen and oxygen atoms. α , β and γ are the angles shown in Figure 1.7. r_2 and r_3 are the distances from the M-site and L-sites to the oxygen atom. q_i is the partial charge and σ and ε are the Lennard-Jones interaction parameters.	19
1.2	Physical properties of the selected water models: the melting temperature, T_M , the temperature of maximum density, T_{MD} , the ratio between the melting point and the critical point, T_M/T_C , the diffusion coefficient at 278 K, D , the dipole μ and the ratio between the dipole moment and total quadrupole moment, μ/Q_T [1].	20
2.1	Summary of the key parameters and results for the simulations performed. ρ is the density in the gas phase, σ is the thickness of the quasi-liquid-layer, τ is the total simulation time, R_{vapor} is the measured growth rate from the vapor phase, and R_{liquid} is corresponding the growth rate from the liquid phase taken from [2]. Representative percentage errors for ρ , σ and R_{vapor} are 15%, 5% and 50%	42

List of Figures

1.1	Water molecule. The direction of its dipole moment is shown with an arrow.	2
1.2	Schematic representation of hydrogen bonding between two water molecules.	3
1.3	Phase diagram for the equilibrium between vapor and liquid phases of water and ice Ih. Adapted from [3].	4
1.4	Unit cell of ice Ih, view from the [0001] and $[11\bar{2}0]$ directions. Adapted from [3].	6
1.5	Hexagonal super cell of ice Ih. Adopted from [3].	7
1.6	The phase diagram of water and ice. Adapted from [4].	8
1.7	Schematic picture of the different water models discussed here. (A) 3-site water model, (B) 4-site water model, and (C) is 5-site water model. Here, the blue and red circles represent the oxygen and hydrogen atoms, respectively, and the green circles represent the negative charge.	18
1.8	Dependence of density on temperature for the selected water models. Asterisks demonstrate experimental value. Squares represent the melting temperatures for each model. The graph is adapted from Ref [5].	21
1.9	Phase diagram of the selected water models: (A) TIP3P, (B) TIP4P and TIP4P/2005, (C) TIP5P, and (D) SPC/E. Experimental symbols are shown for comparison. Frames (A), (B) and (C) are adapted from Ref. [5] and figure (D) is adopted and modified from Ref. [6].	22
2.1	Snapshot from the configuration of the equilibrated system taken from the basal simulation at 245 K. Hydrogen and oxygen atoms are represented in white and red colors, respectively.	34
2.2	Density and temperature profiles for the initial state of the simulation on the basal face at 245 K.	35
2.3	Comparison between the average density and temperature profiles for the simulation on the basal face at 245 K.	36
2.4	Average density and RMSD profiles along the Z-axis for one of the simulations on the basal face at 245 K. The inset graph shows the same comparison near the gas - QLL interface (-15 to -12 Å).	39
2.5	The averaged density and potential energy profiles at the interface for one of the simulations on the basal face at 245 K.	40

2.6	The time evolution of the position of the growing ice surface for the simulation on the prism face at 220 K. The positions are along the Z-axis in the lab frame.	43
2.7	The average density profiles at the selected temperatures as a function of distance from the growing basal face of ice. The QLL thickness values for simulations at 220, 235, and 245 K are 8.8 Å, 9.1 Å, and 12.4 Å, respectively.	44
2.8	The average density profiles at the selected temperatures as a function of distance from the growing prism face of ice. The QLL thickness values for simulations at 220 and p245 K are 7.6 Å and 10.2 Å, respectively.	45
2.9	Results for the QLL thicknesses on the basal and prism faces obtained in this work in comparison with those obtained from ref. [7] as a function of the undercooling.	46
2.10	Comparison of the average density profiles for the basal and prism faces at 220 K.	47
2.11	Average density profiles and instantaneous configurations obtained from the a) b220 and b) p220 simulations. The snapshots are taken normal to the direction of the growing ice surface. The vertical blue solid line represents the position of the ice surface determined by the MD code. Here, oxygen and hydrogen atoms are represented in red and white colors, respectively.	48
2.12	The average density profiles for the basal simulations at 245 K with densities in the gas phase of 20, 9, and 6 mol/m ³ , respectively. The QLL thicknesses for the b245-1, b245-2 and b245-3 systems are 12.4 Å, 9.8 Å, and 8.8 Å, respectively.	49
2.13	Comparison between the average density profile for the b245-1 system and an instantaneous configuration from the same simulation. The snapshot is taken normal to direction of the growing ice surface. The vertical blue solid line represents the interface Z coordinate calculated by the MD code. The oxygen and hydrogen atoms are represented in red and white colors, respectively.	50
A.1	The time evolution of the position of the surfaces for the simulation on the basal face at 220 K. The positions are along the Z-axis in the lab frame.	62
A.2	The time evolution of the position of the surfaces for the simulation on the basal face at 235 K. The positions are along the Z-axis in the lab frame.	62
A.3	The time evolution of the position of the surfaces for the simulation on the basal face at 245 K. The positions are along the Z-axis in the lab frame.	63

A.4	The time evolution of the position of the surfaces for the simulation on the prism face at 220 K. The positions are along the Z-axis in the lab frame. . .	63
A.5	The time evolution of the position of the surfaces for the simulation on the prism face at 235 K. The positions are along the Z-axis in the lab frame. . .	64
A.6	The time evolution of the position of the surfaces for the simulation on the prism face at 245 K. The positions are along the Z-axis in the lab frame. . .	64
A.7	the averaged density and potential energy profiles a) for the whole system and b) in the gas phase for one of the simulations on the basal face at 245 K.	65
A.8	Average density profiles and instantaneous configurations obtained from the b235 simulation. The snapshots are taken normal to the direction of the growing ice surface. The vertical blue solid line represents the position of the ice surface determined by the MD code. Here, oxygen and hydrogen atoms are represented in red and white colors, respectively.	66
A.9	Average density profiles and instantaneous configurations obtained from the p235 simulation. The snapshots are taken normal to the direction of the growing ice surface. The vertical blue solid line represents the position of the ice surface determined by the MD code. Here, oxygen and hydrogen atoms are represented in red and white colors, respectively.	67
A.10	Average density profiles and instantaneous configurations obtained from the p245 simulation. The snapshots are taken normal to the direction of the growing ice surface. The vertical blue solid line represents the position of the ice surface determined by the MD code. Here, oxygen and hydrogen atoms are represented in red and white colors, respectively.	68
A.11	Comparison of the average density profiles for the basal and prism faces at 245 K.	68

Chapter 1

INTRODUCTION

1.1 Introduction

Ice plays an important role in many atmospheric and environmental phenomena on Earth [8–10]. Formation and growth of atmospheric ice crystals govern many properties of clouds [10]. Understanding the ice growth from vapor at the molecular-scale helps to provide a better perception of climate and atmospheric processes. In addition, according to our everyday experiences, we know that the ice surface is slippery, which due to the liquid – like surface of ice, where the ice surface melts below the bulk melting point [8]. The characteristics of this premelted layer are different from those of liquid water and so, it is commonly called the quasi – liquid layer. The nature and different properties of this quasi – liquid layer are the subjects of many studies in chemistry, astronomy and geophysics [8, 11–13] as it plays a significant role in the phenomenon of ice growth from the vapor [14].

In this thesis, molecular dynamics simulations have been employed to maintain steady – state ice growth from water vapor and investigate the dependence of the behavior of the quasi – liquid layer that forms on the ice surface on various factors including temperature, ice face and flux of particles in the gas. To the best of my knowledge, due to lack of an appropriate model, there has been no research published in the literature which explores this phenomenology from a microscopic point of view. In this work, a methodology has been introduced to demonstrate proof of principle for obtaining a steady – state molecular simulation of the ice growth from the vapor phase. I hope this study provides the groundwork for future investigations in this field.

The structure of the thesis is organized as follows. In chapter 1, background and theory used in this work are introduced where section 1.2 provides the properties and structure of ice and water, in section 1.3 and 1.4 the molecular dynamics method and the choice of water model are explained and in section 1.5 the relevant important theoretical and experimental

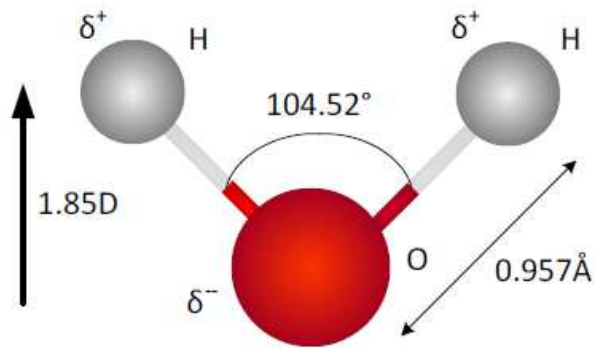


Figure 1.1: Water molecule. The direction of its dipole moment is shown with an arrow.

studies previously reported in the literature are reviewed. Chapter 2 reports the results of new simulations, in which the simulation setup and preparation are explained in section 2.1, and the results of different simulations on ice growth from water vapor are presented in section 2.2. Finally, the conclusions and suggestions for future works are provided in Chapter 3.

1.2 Water and ice properties

Water is the most important substance for our life and has been under continuous attention by scientists due to its unique and unusual properties. For instance, the temperature at which water has its maximum density is above its melting point and the density of the normal form of ice, ice Ih, is lower than that of liquid water. In addition, for this relatively small molecule, the melting point is unusually high as compared to other compounds. Also, water can exist in various crystalline forms [3, 8]. In this section, an overview of different properties of water and its various solid forms is provided.

1.2.1 Water

In a water molecule, with molecular formula H_2O , two hydrogen atoms are covalently bonded to an oxygen atom. As it is shown in Figure 1.1, the equilibrium distance between

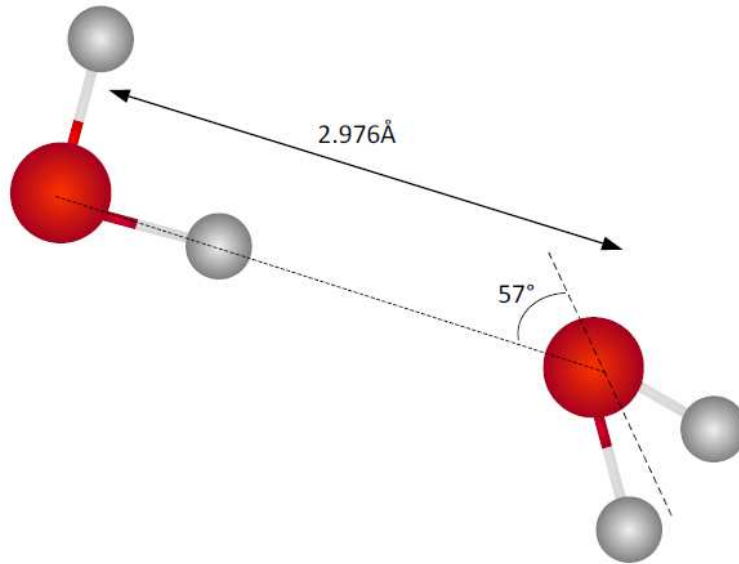


Figure 1.2: Schematic representation of hydrogen bonding between two water molecules.

the oxygen and hydrogen atoms is about 0.957 \AA and the angle between the oxygen and hydrogen bonds is about 104.52° [3]. Water is a polar molecule. The high electronegativity of the oxygen atom leads to an uneven electron density distribution in a water molecule where it is more concentrated near the oxygen atom. Consequently, there is a partial negative charge, δ^- , near the oxygen atom and partial positive charges δ^+ on the hydrogen atoms. In the gas phase the dipole moment in a water molecule is 1.85 Debye [15]. This uneven electron density of water molecules results in an attractive interaction between them, known as hydrogen bonding.

Hydrogen bonds are known to be responsible for many of the unique properties of the different phases of water such as its relatively high boiling temperature, the temperature of the maximum density of water, the lower density of ice relative to water, and the tetrahedral structure of water [3,8]. The hydrogen bonding in a water dimer is represented in Figure 1.2, where one water molecule is oriented in a way that its positively charged hydrogen atom lies between two negatively charged oxygen atoms, one from the same molecule and one from another water molecule. The energy of a hydrogen bond is generally considered to consist of different contributions. If two water molecules are brought together, there will be

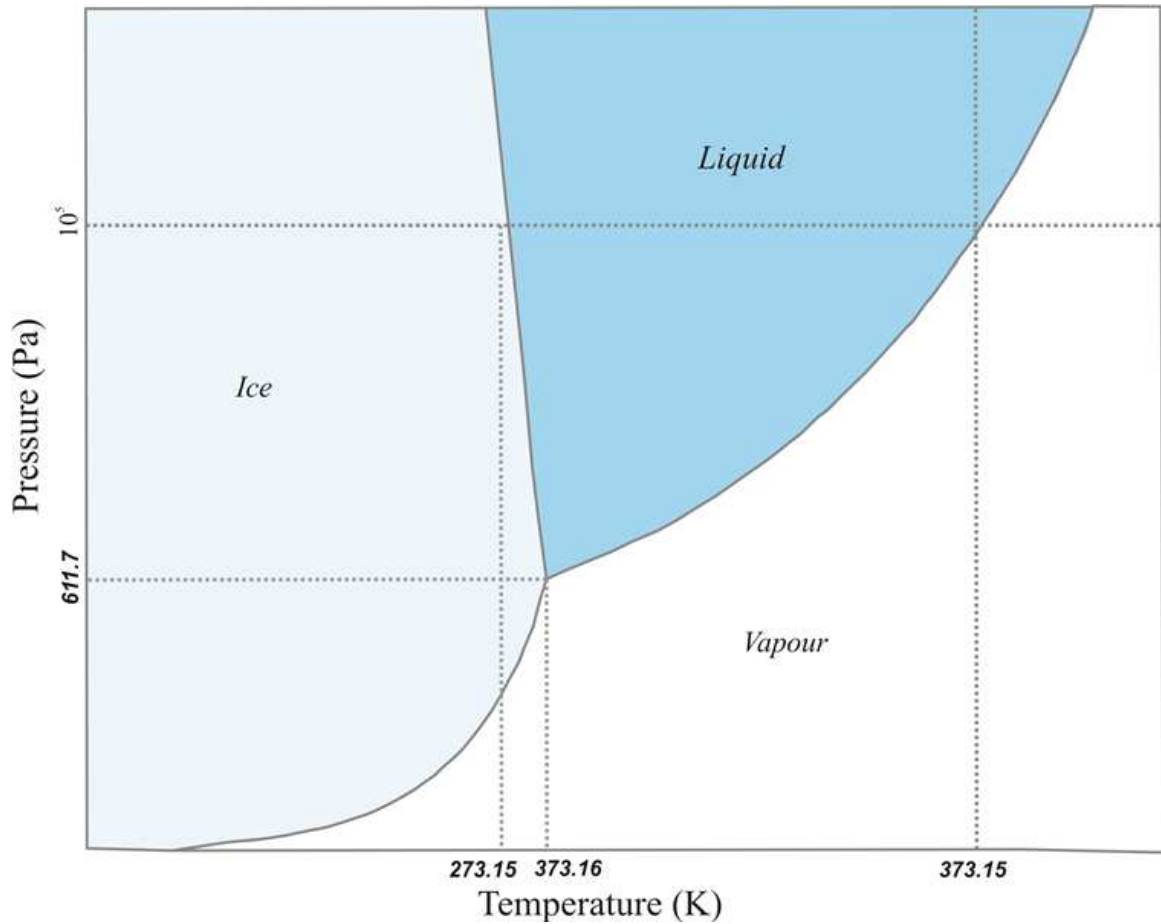


Figure 1.3: Phase diagram for the equilibrium between vapor and liquid phases of water and ice Ih. Adapted from [3].

electrostatic interactions between their partial charges. By bringing together two molecules, they also polarize each other, that is there is a distortion of their charge distributions. All of these effects strengthen the hydrogen bond. However, interpenetration of the charge clouds may violate the Pauli exclusion principle which results in a repulsive force. The energy of a hydrogen bond in ordinary ice is about $23 \frac{KJ}{mol}$ [16]. There can be up to four hydrogen bonds formed by one water molecule: its two hydrogen atoms can form hydrogen bonds with two neighbors, while it accepts two hydrogen bonds from two other neighbors.

1.2.2 Hexagonal ice Ih

Figure 1.3 demonstrates the phase diagram for the equilibrium between vapor and liquid phases of water and ice Ih. Ice Ih is the hexagonal form of ice which is stable under atmospheric pressure conditions [8]. The water molecules of ice Ih are arranged in a hexagonal lattice structure in a way that each molecule establishes four H – bonds with the molecules surrounding it. Positions of atoms in an ice Ih lattice obey the Bernal-Fowler rules [3]:

- Each oxygen atom is directly attached to two hydrogen atoms forming a water molecule.
- Two hydrogen atoms of one molecule are directed towards two other oxygen atoms in neighboring molecules.
- Only one hydrogen atom is located between two oxygen atoms in the lattice structure.
- Different configurations for ice Ih are based on the distribution of hydrogen atoms relative to the oxygen atoms.

Many of the mechanical and electrical properties of ice Ih originate from the disordered distribution of hydrogen atoms between oxygen atoms. One of the consequences of the ice Ih structure and tetrahedral arrangement of the water molecules is the low density of ice in comparison with liquid water under atmospheric conditions [3].

Figure 1.4 shows the unit cell of the ice Ih lattice which consists of four water molecules. As was mentioned before, following the Bernal-Fowler rules, there is one hydrogen atom between each pair of oxygen atoms. In Figure 1.4 there are two sites for each hydrogen atom to demonstrate the proton-disordered behavior of the hexagonal ice. The unit cells pack into a hexagonal super cell as is shown in Figure 1.5. The hexagonal ice structure can be seen to consist of hexagonal layers stacked on top of each other in an ABAB pattern. The face that is perpendicular to the C-axis, identified with a (0001) notation, is known as the basal face. The faces which are parallel to the C-axis are the prism faces of ice Ih. There are two sets of prism faces: primary and secondary and they are represented with (10-10) and (1-210) notations, respectively. Another set of planes in ice Ih are known as pyramidal faces. In this work, the growth on primary faces (basal and prism) of hexagonal

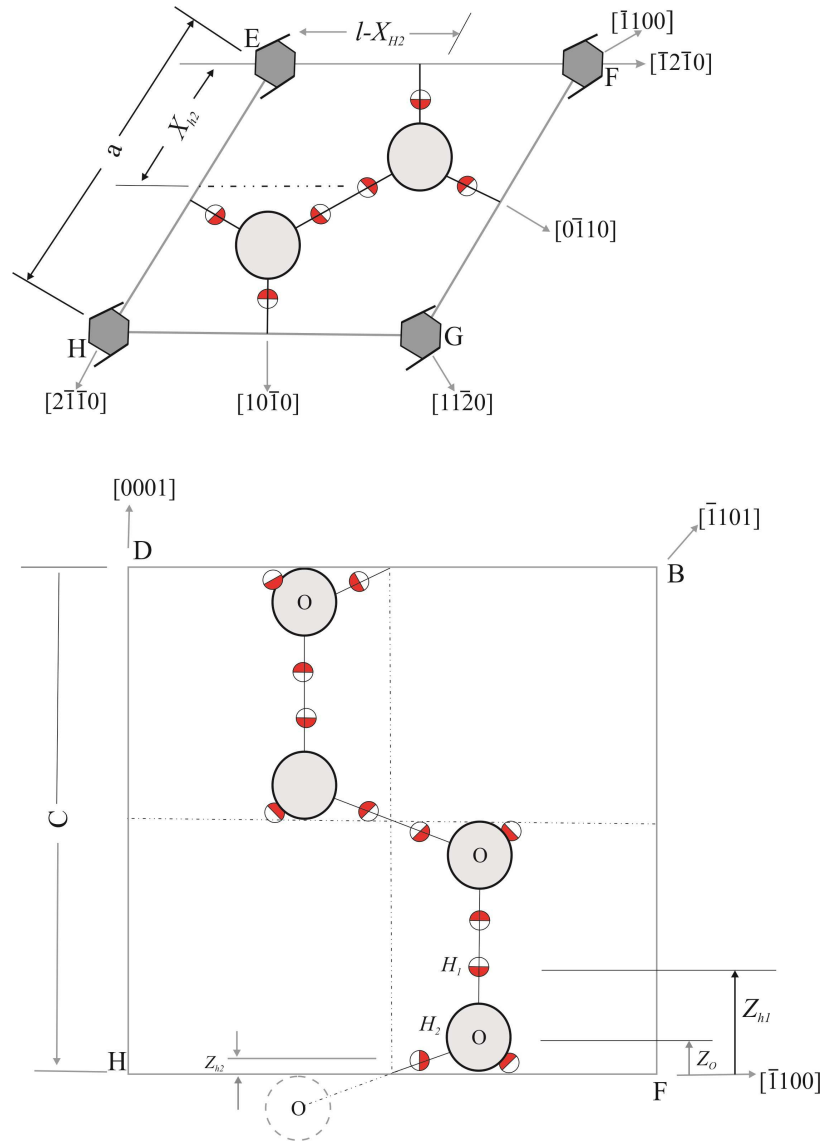


Figure 1.4: Unit cell of ice Ih, view from the $[0001]$ and $[11\bar{2}0]$ directions. Adapted from [3].

ice will be investigated.

1.2.3 The other phases of ice

There are two thermodynamically different phases of ice: stable and metastable [3]. Apart from ice Ih, which is the stable form of ice under atmospheric pressure, there are various phases of ice that are mostly produced under increased pressure. High pressure deforms the hydrogen bonds in ice which leads to a denser structure. There is a metastable form of

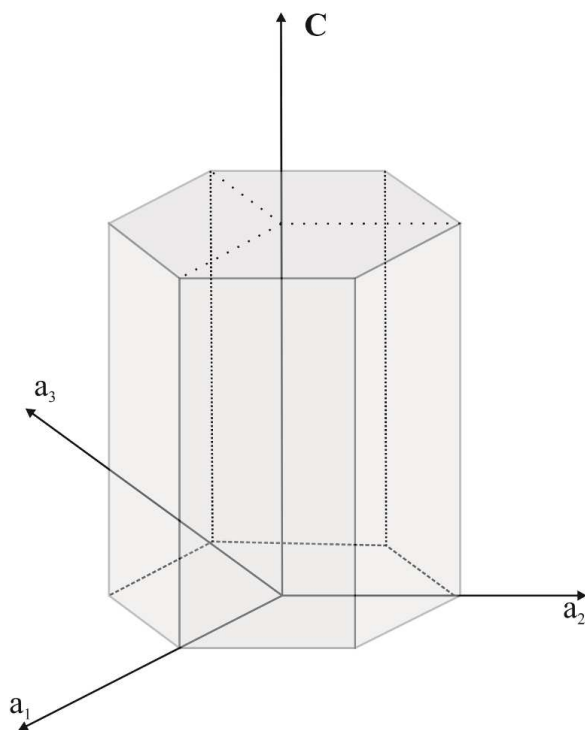


Figure 1.5: Hexagonal super cell of ice Ih. Adopted from [3].

ice under atmospheric pressure known as ice Ic or cubic ice with similar lattice properties to ice Ih [3, 8]. Water molecules in cubic ice are four-fold coordinated with ABC – ABC stacking of hexagonal layers. However, its lattice structure is cubic as compared with the hexagonal structure of ice Ih. The unit cell of cubic ice has eight water molecules. Ice Ic can be considered as an intermediate phase of ice in transformation from other phases to stable ice Ih [3, 17, 18].

The phase diagram in Figure 1.6 shows different phases of ice (ice polymorphs). It was proposed by Tammann [19] and Bridgman [20] to label ice polymorphs with Roman numerals. There are currently fifteen different phases of ice experimentally characterized and reported in the literature [4].

Although the existence of the high-pressure phases of ice on Earth has not been shown yet, only ices II, III, VI and VII among them can potentially be found on our planet [18]. More details of the structure and different properties of ice polymorphs can be found in the literature [3, 8, 18].

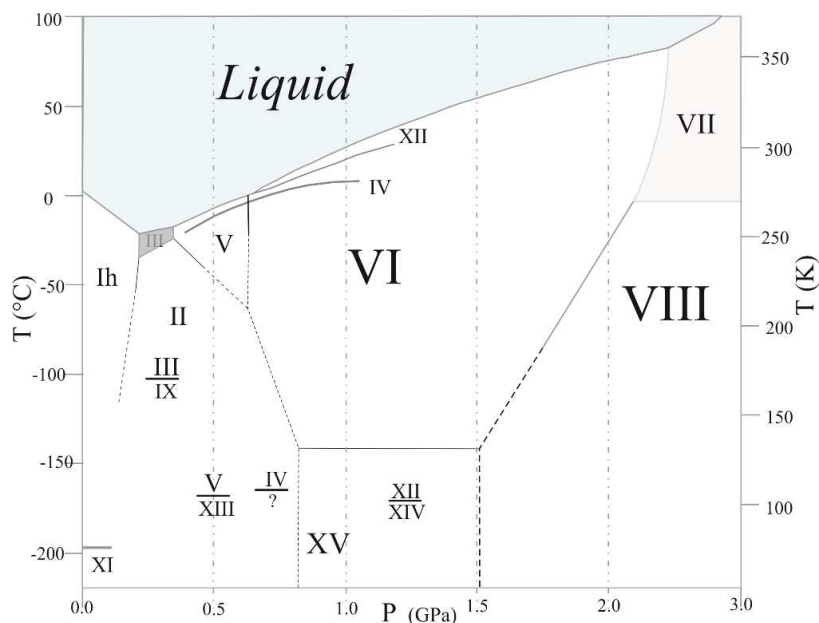


Figure 1.6: The phase diagram of water and ice. Adapted from [4].

1.2.4 Ice-vapor interface

The ice-vapor interface plays an important role in the growth behavior of ice from vapor. It has been shown by experimental and theoretical studies that many of the properties of ice, such as its growth rate, or adsorption or desorption processes on its surface are governed by the surface premelting of ice, known as a quasi-liquid-layer (QLL) [14, 21, 22]. It has been demonstrated that the quasi-liquid-layer forms on the ice surface at temperatures above ~ 150 -180 K and its thickness depends on temperature and varies for different faces of ice Ih [7]. One of the objectives of this work was to monitor how the QLL thickness changes for basal and primary prism faces of ice at temperatures close to the melting point and how this thickness might impact the growth behavior.

1.3 Molecular dynamics

As one of the most powerful tools to investigate the structure and dynamics of molecular systems microscopically [23], the molecular dynamics method was chosen in this work to study the phenomenon of ice growth from water vapor. This method requires integrating

Newtonian equations of motion, $F = ma$, where F represents the force applied on a particle in the system, and m and a are its mass and acceleration, respectively. To solve the equations of motion for different particles one should know about the potential energies and positions as acceleration is the second temporal derivative of position and force is the derivative of potential energies with respect to distance. In principle, if the initial state of a system is known, its state at any other time can be predicted by solving the Newtonian equations of motion [23]. If there are many particles in the system (many-body problem), it is impossible to solve the equations of motion analytically [23] and numerical approaches are employed. In such cases, the integration involves expanding the positions of particles in Taylor series,

$$r(t + \delta t) = r(t) + v(t)(\delta t) + \frac{1}{2}a(t)(\delta t)^2 + \frac{1}{6}b(t)(\delta t)^3 + \dots \quad (1.1)$$

It is assumed that the time interval, δt , is short and the forces are constant during this time. The forces acting on particles (atoms or molecules) are calculated and combined with the initial positions $r(t)$ and velocities $v(t)$ to find the new positions and velocities after δt . Then, the particles are displaced to the new positions and forces are updated accordingly.

The sets of velocities and positions of particles calculated over a period of time produce a trajectory that describes the evolution of the system with time. Since each particle has three Cartesian coordinates and three components of momentum, it can be described by six variables. Therefore, in the case of a many-body system, the set of velocities and positions form a $6N$ dimensional space named phase space. The system samples a specific set of points in its phase space based on the applied conditions such as constant pressure, temperature, number of particles or volume. These collections of points (sets of positions and velocities) are known as ensembles. In this study, the systems sample their phase space in two different ensembles, isobaric-isothermal ensemble during the preparation stage and canonical ensemble in the production stage. In an isobaric-isothermal ensemble, the number of particles (N), the pressure (P), and the temperature (T) are kept constant. This ensemble is abbreviated as the NPT ensemble. In a canonical ensemble, the number of particles (N),

the volume (V), and the temperature (T) are kept constant. This ensemble is abbreviated as the NVT ensemble [23].

In molecular dynamics simulations, macroscopic properties of a system can be calculated by averaging over their instantaneous values over time. As the measurement time approaches infinity, this can be written as [23]:

$$\langle A \rangle_{time} = \lim_{\tau \rightarrow \infty} \frac{1}{\tau} \int_{t=0}^{\tau} A(p^N(t), r^N(t)) dt, \quad (1.2)$$

where A is the macroscopic quantity, $\langle \rangle_{time}$ indicates the time average, τ is the simulation time, and $A(p^N(t), r^N(t))$ is the instantaneous value of A corresponding to the positions and momenta of particles.

However, simulations of macroscopic systems (with macroscopic dimensions and number of particles) are not practical. Thus, the time average can be substituted with an ensemble average [23]:

$$\langle A \rangle = \iint dp^N dr^N A(p^N, r^N) \rho(p^N, r^N), \quad (1.3)$$

where $\langle \rangle$ means the ensemble average, and $\rho(p^N, r^N)$ is the probability density of the ensemble. This density provides the probability of finding the system in a configuration with particular positions and momenta. In this way of averaging, the system evolving over time is substituted with a large number of its replicas simultaneously [23].

A system in MD studies typically contains hundreds or thousands of particles in a simulation box with dimensions of the order of tens or hundreds of angstroms. In order to study the bulk properties of such a microscopic system one needs to overcome the boundary effects which otherwise would prevent it from representing a macroscopic system of interest appropriately. One solution to this problem is choosing periodic boundary conditions (PBC) for the system [23]. By applying periodic boundary conditions, estimates for bulk properties can be calculated from systems with a relatively small number of particles.

In PBC, the simulated system is surrounded by an infinite number of replicas of itself in all directions, and consequently as one particle leaves the box from one side, it is replaced by its replica from the opposite side so that the number of particles remains constant [23].

As previously mentioned, molecular dynamics simulations involve solving the equations of motion based on the forces among particles at each simulation step. These forces are derivatives of potential energies with respect to distance. In these simulations, all water molecules are treated as rigid molecules and with no internal degrees of freedom (for details on the selected water model please see Section 2.1). In rigid model simulations, the potential energy is only the sum over non-bonded interactions. Non-bonded interactions can be described by van der Waals and electrostatic interactions between the interaction sites. The van der Waals interactions are described in the form of a Lennard-Jones potential [23]:

$$u_{ij}^{LJ} = 4\epsilon\left[\left(\frac{\sigma}{r_{ij}}\right)^{12} - \left(\frac{\sigma}{r_{ij}}\right)^6\right], \quad (1.4)$$

where σ and ϵ are known as the collision diameter (or the linear dimension of the site) and the well depth, respectively, and r_{ij} is the distance between the interaction sites. In Eq. 1.4, the first term describes the short-range repulsive part and the second term corresponds to longer-range attractive forces between particles. σ and ϵ are adjustable parameters and vary depending on atom types. They can be defined for interactions between particles of either the same or different kinds. For two different sites, A and B, the corresponding parameters σ_{AB} and ϵ_{AB} can be estimated using different combination rules, such as geometric:

$$\epsilon_{AB} = \sqrt{\epsilon_A \epsilon_B}, \quad (1.5)$$

and

$$\sigma_{AB} = \sqrt{\sigma_A \sigma_B}, \quad (1.6)$$

or Lorentz-Berthelot

$$\epsilon_{AB} = \sqrt{\epsilon_A \epsilon_B}, \quad (1.7)$$

and

$$\sigma_{AB} = \frac{\sigma_A + \sigma_B}{2}, \quad (1.8)$$

The electrostatic interactions between point charges which represent the interactions between the partial charges of the molecule are given by Coulomb's law. When periodic boundary conditions are applied, it is expressed with the following formula:

$$u_{ij} = \frac{1}{2} \sum_{|n|=0} \sum_{i=1}^N \sum_{j=0}^N \frac{1}{4\pi\epsilon_0} \frac{q_i q_j}{|r_{ij} + nL|}, \quad (1.9)$$

where q_i and q_j are the point charges, ϵ_0 is the permittivity of vacuum ($8.85 \times 10^{-12} \frac{\text{farad}}{\text{m}}$), r_{ij} is the distance between the charges, $n(=n_1L, n_2L, n_3L)$ is the image box index and L is the length of the box. It should be noted that in this equation, the interactions between $i = j$ for $n = 0$ are ignored. Also, the factor $\frac{1}{2}$ is introduced to correct for the double-counting. Eq. 1.9 converges conditionally and would represent a problem to simulations. To avoid this problem, the Ewald summation method [23, 24] is commonly utilized. In this method, each point charge is surrounded in real space by a charge distribution of the Gaussian form which has equal size but opposite sign. Also, there is another Gaussian distribution in the reciprocal space to cancel out the first one. Introducing the Gaussian charge distributions makes the electrostatic potential converge much more rapidly and allows the simulations to proceed efficiently [23].

In the evaluation of forces, the non-bonded potential terms between every pair of particles must be calculated. The calculation of non-bonded potential energies is the most time consuming step in a molecular dynamics simulation [23]. To speed up the simulation, a cut-off distance is usually taken into account so that the interaction between the particle of interest and the other particles is assumed to be negligible at distances greater than the

assigned cut-off and it is ignored [23]. More details on different ways to define the cut-off distance can be found in standard references [23, 24].

1.3.1 Constant temperature control

The production simulations in this work were performed in the canonical ensemble. In order to control temperature at the desired value, Nosé-Hoover chain thermostats were used [25, 26]. In this part, a brief introduction to this technique is provided. More detailed overviews of various methods employed for controlling the temperature in MD simulations can be found in the literature [23, 25, 27–29].

In experimental studies, it is often difficult to control the total energy of the physical system and it is usually the temperature that is kept constant through the exchange heat between the system of interest and a much larger system with known temperature (the heat bath). In a simulation, in order to achieve a constant temperature, one must allow for this heat flow in the system. It is known that the temperature of a system is directly connected to the time average of the kinetic energy. Thus, one way to control the temperature is to rescale the velocities of the particles in the system. Another approach is to couple the system to a thermal reservoir, known as thermostat. In the approach of Nosé [28, 30] the heat bath is introduced to the system as an extra degree of freedom s . The extended system which consists of N particles is described by the Hamiltonian function [31]

$$H_{Nosé} = \sum_i^N \frac{\mathbf{p}_i^2}{2m_i s^2} + U(q^N) + \frac{\mathbf{p}_s^2}{2Q} + g k_B T \ln(s), \quad (1.10)$$

where p_i is the momentum related to the general coordinate (q_i) of the particle i with the mass of m_i , g represents the number of degrees of freedom of the system, U is the potential energy, T is the temperature, k_B is Boltzmann's constant, s and p_s are parameters related to the heat bath, and Q is the *effective mass* of the heat bath. In the approach of Nosé the time step is scaled by s [32]. Hoover [29] has shown that the equations of motion derived from the Nosé hamiltonian can be simplified in order to avoid the time scaling

$$\dot{\mathbf{q}}_i = \frac{\mathbf{p}_i}{m_i}, \quad (1.11)$$

$$\dot{\mathbf{p}}_i = \mathbf{F}_i - \xi \mathbf{p}_i, \quad (1.12)$$

$$\dot{\xi} = \dot{s}/s, \quad (1.13)$$

$$\dot{\xi} = \frac{\sum_i \frac{\mathbf{p}_i^2}{m_i} - gk_B T}{Q}, \quad (1.14)$$

where $\xi = \mathbf{p}_s/Q$ is the thermodynamic friction coefficient. The Eq. 1.11 and Eq. 1.12 are the equations of motion for the particle i in the system and Eq. 1.13 and Eq. 1.14 are those associated with the heat bath. The Nosé-Hoover thermostat achieves the canonical distribution if the system of interest is ergodic [25]. If the dynamics is not ergodic for small or stiff systems, this method does not generate a correct distribution [29]. To help ensure ergodic behavior, the Nosé-Hoover chain method has been introduced by Martyna and coworkers [25]. In this method, Nosé thermostating is applied on the thermostat itself so that the size of the extended system increases which helps in achieving ergodic behavior. The equations of motion in the Nosé - Hoover chain method are

$$\dot{\mathbf{q}}_i = \frac{\mathbf{p}_i}{m_i}, \quad (1.15)$$

$$\dot{\mathbf{p}}_i = \mathbf{F}_i - \mathbf{p}_i \frac{P_{\xi_1}}{Q_1}, \quad (1.16)$$

$$\dot{\xi}_k = \frac{P_{\xi_k}}{Q_k}, \quad (1.17)$$

$$\dot{p}_{\xi_1} = \left(\sum_i \frac{\mathbf{p}_i^2}{m_i} - gk_B T \right) - \frac{p_{\xi_2}}{Q_2} p_{\xi_1}, \quad (1.18)$$

$$\dot{p}_{\xi_k} = \left[\frac{p_{\xi_{k-1}}^2}{Q_{k-1}} - k_B T \right] - \frac{p_{\xi_{k+1}}}{Q_{k+1}} p_k, \quad (1.19)$$

$$\dot{p}_{\xi_M} = \left[\frac{p_{\xi_{M-1}}^2}{Q_{M-1}} - k_B T \right], \quad (1.20)$$

where M thermostats have been included in the chain and in Eq. 1.17 $k = 1, \dots, M$. The addition of extra thermostats forms a simple one - dimensional chain which is relatively inexpensive to treat computationally. The values of the thermostat masses (Q_i) should be chosen with care in order for the dynamics of the system to achieve the canonical distribution [25, 29, 33]. In the Nosé-Hoover chain thermostats that are used in this work, each particle is coupled to four bath reservoirs connected to each other. Also, the translational and rotational temperatures for each particle are controlled by two separate thermostats [34].

1.3.2 Constant pressure control

Many experimental studies are performed under isothermal-isobaric conditions and in order to make direct comparison with experimental data it is favorable to conduct simulations at constant temperature and pressure. Indeed, the NPT ensemble was used in the preparation step of these simulations. Here, the pressure control used in this work is briefly explained.

Pressure is determined in a simulation through the virial theorem which is calculated as the sum of the product of the particle coordinates and the derivative of the potential energy functions [23, 27]:

$$W = \sum r_{ij} \left(\frac{dU(r_{ij})}{dr_{ij}} \right), \quad (1.21)$$

where r_{ij} is the relative particle coordinate and $U(r_{ij})$ is the potential energy between par-

ticle i and j . Based on the virial theorem, this product is equal to $-3Nk_B T$, where N is the number of particles, k_B is the Boltzmann constant, and T is the temperature. For a real gas, the virial has two parts: the ideal gas term ($-3PV$), and the non-ideal portion. So, the pressure can be given as:

$$P = \frac{1}{V} [Nk_B T - \frac{1}{3} \sum_{i=1}^N \sum_{j=i+1}^N r_{ij} (\frac{dU(r_{ij})}{dr_{ij}})]. \quad (1.22)$$

In simulations, the isothermal-isobaric ensemble is achieved by changing the volume of the simulation cell. Similar to the temperature control approach, one widely used method to maintain constant pressure is to couple the system to a pressure bath (barostat). In this work, the Berendsen barostat is used in the preparation step [23, 27]. In a Berendsen barostat, the rate of change in the volume of the system is given by:

$$\frac{dV(t)}{dt} = \frac{1}{\tau_p} (P_{bath} - P(t)), \quad (1.23)$$

where τ_p is the coupling constant, $P(t)$ is the actual pressure at time t , and P_{bath} is the pressure of the bath. Then, the volume is scaled using a factor given by:

$$\lambda = 1 - \kappa \frac{\partial t}{\tau_p} (P - P_{bath}), \quad (1.24)$$

where ∂t is the time step of the simulation and κ is the isothermal compressibility of the system. The atomic coordinates are then rescaled by a factor of $\lambda^{1/3}$ to achieve a target average pressure.

1.4 Water models

In the previous section, the essential concepts of the molecular dynamics method have been reviewed. As the main objective of this work is to study the growth of ice from vapor, an appropriate water model that can reproduce various properties of water and ice is required to be employed in these simulations. In this section, different rigid, non – polarizable water

models are reviewed and the choice of the water model for the simulations in this work is explained.

From a microscopic point of view, the charge distribution on the water molecule and the many body interactions between them are responsible for different properties of water. The quality of the simulations performed on water depends significantly on the choice of water potential model which parameterizes the interactions between molecules. An ideal computational model should be able to predict different properties of water in different phases. During the last couple of decades, various models have been developed and used in numerous molecular dynamics simulations of water [1, 5, 35–37]. While some of these models were polarizable, in others an effective charge distribution was chosen to mimic its polarizability. Some have rigid geometry and some are flexible. Indeed, different methods were utilized to deal with the potential energy in this environment. *Ab-initio* water models incorporate the electronic structure to find the potential energy of the system. Another class of models, which are known as coarse-grain models, use softer interactions and represent water molecules or groups of water molecules in single sites [37].

Coarse-grained and *ab-initio* models can be considered as examples at two ends of the range of possible water models. While *ab-initio* models are more realistic and allow for bond making and breaking, at the other end of this range, coarse-grain models allow for much longer time- and length-scale simulations to be performed. Empirical models are somewhere in between. Compared with the *ab-initio* models, the empirical models are computationally much less demanding while they still look to retain the molecular nature of the interactions within a water system (e.g. the specifics of the H-bonds) and they determine the interactions more precisely as compared with coarse-grained water models.

A literature review on rigid, non-polarizable models shows that this type of water model is well tested and some of them perform well in describing different properties of water [5]. In addition, these models are computationally much less expensive than polarizable or flexible models [1]. Therefore, in order to obtain reasonable results in this study at a

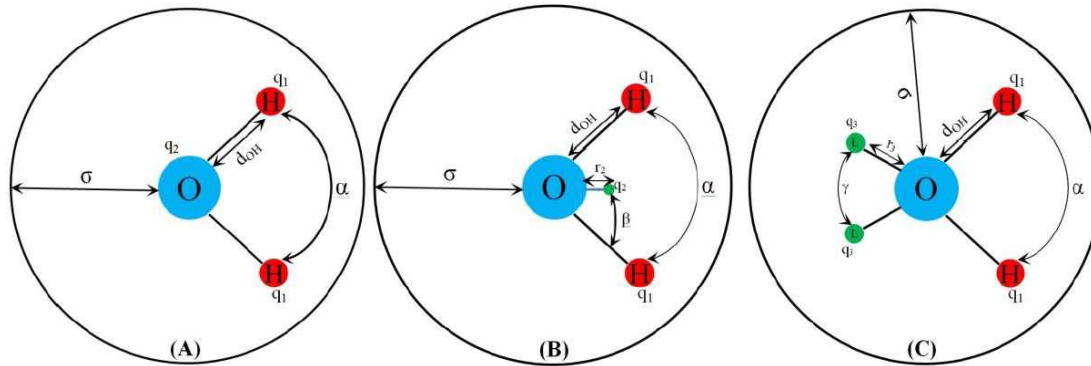


Figure 1.7: Schematic picture of the different water models discussed here. (A) 3-site water model, (B) 4-site water model, and (C) is 5-site water model. Here, the blue and red circles represent the oxygen and hydrogen atoms, respectively, and the green circles represent the negative charge.

reasonable computational cost, the most popular and well known rigid, non-polarizable water models will be reviewed with respect to their prediction of different properties of water to guide the selection of a model. For this purpose, the focus will be on TIPnP-like and the SPC/E models. By the TIPnP-like models I mean TIP3P, TIP4P, TIP5P and TIP4P/2005. Figure 1.7 provides a schematic representation for the different water model structures.

The water models in this category have the same bond geometry, i.e. the d_{OH} and H-O-H angle in these models are 0.9572 \AA and 104.52° , respectively. In addition, in all of them, a Lennard-Jones interaction site is located on the position of the oxygen atom and a positive charge is on each of the hydrogen atoms [5]. Table 1.1 summarizes different parameters of the water models that are discussed in this section.

The TIP3P model [42] is a three site model in which the negative charge is located on the oxygen atom. This model is mostly used in simulations on biological systems. The force field parameters of this model were optimized to reproduce the vaporization enthalpy and the liquid density of water at room temperature. There are nine distances to be computed between sites of two water molecules in the TIP3P potential model, which reflects the computational cost for this model [5].

<i>Model</i>	<i>Type</i>	d_{OH} (Å)	$\alpha\beta\gamma$ (deg.)	r_i (Å)	q_i (a.u.)	σ (Å)	ϵ/k_B (K)	<i>Ref.</i>
<i>TIP3P</i>	<i>A</i>	0.9572	$\alpha=104.52$	-	$q_1=0.4238$ $q_2=-0.8476$	3.1506	76.54	[38]
<i>SPC/E</i>	<i>A</i>	1.0	$\alpha=109.47$	-	$q_1=0.4238$ $q_2=-0.8476$	3.1656	78.20	[39]
<i>TIP4P</i>	<i>B</i>	0.9572	$\alpha=104.52$ $\beta=52.26$	$r_2=0.1546$	$q_1=0.520$ $q_2=-1.040$	3.1540	78.02	[38]
<i>TIP5P</i>	<i>C</i>	0.9572	$\alpha=104.52$ $\gamma=109.47$	$r_3=0.700$	$q_1=0.2410$ $q_3=-0.2410$	3.1200	80.51	[40]
<i>TIP4P/2005</i>	<i>B</i>	0.9572	$\alpha=104.52$ $\beta=52.26$	$r_2=0.1546$	$q_1=0.5564$ $q_2=-1.1128$	3.1589	93.2	[41]

Table 1.1: Potential parameters of discussed water models. The type of water model corresponds to the schematic representations in Figure 1.7. d_{OH} is the distance between hydrogen and oxygen atoms. α , β and γ are the angles shown in Figure 1.7. r_2 and r_3 are the distances from the M-site and L-sites to the oxygen atom. q_i is the partial charge and σ and ϵ are the Lennard-Jones interaction parameters.

In the TIP4P model [42] the negative charge (M-site) is not on the position of the oxygen atom but shifted toward the hydrogen atoms (see (B) in Figure 1.7). Similarly to the TIP3P model, the parameters of TIP4P were optimized to reproduce the density of liquid water and the vaporization energy at ambient conditions. Indeed, to deal with the massless interaction site (M-site) may cause some difficulties in molecular dynamics codes. In addition, using this water model is computationally more demanding as compared with the TIP3P model since it requires the evaluation of 10 site-site interactions [5].

In the 5-site TIP5P model [40], the location of the negative charges is changed to the positions of the two electron lone pair sites of oxygen (L-sites). In addition to the vaporization enthalpy and density of liquid water at ambient conditions, the parameters of this model were optimized to reproduce the maximum density of liquid water. As TIP5P has five interaction sites (four point charges and one Lennard-Jones interaction site), it has 17site-site interactions to evaluate.

The most recent water model in this category is TIP4P/2005 [41] which is a modified version of the TIP4P model. While the TIP4P model can qualitatively describe the phase

<i>Model</i>	T_M (K)	T_{MD} (K)	T_M/T_C	$\ln D$ (278 K)	μ (D)	μ/Q_T (\AA^2)	<i>Ref.</i>
<i>TIP3P</i>	146	182	0.251	-10.2	2.350	1.363	[5, 43]
<i>SPC/E</i>	215	241	0.337	-11.08	2.350	1.155	[5, 43]
<i>TIP4P</i>	232	253	0.394	-10.78	2.177	1.014	[5, 43]
<i>TIP5P</i>	274	277	0.525	-11.41	2.290	1.460	[5, 43]
<i>TIP4P/2005</i>	252	278	0.394	-11.27	2.305	1.004	[5, 41]
<i>Expt. value</i>	273.15	277	0.422	-11.24	1.85 (Gas)	0.721	[5]

Table 1.2: Physical properties of the selected water models: the melting temperature, T_M , the temperature of maximum density, T_{MD} , the ratio between the melting point and the critical point, T_M/T_C , the diffusion coefficient at 278 K, D , the dipole μ and the ratio between the dipole moment and total quadrupole moment, μ/Q_T [1].

diagram of water, it still predicts a rather low melting temperature. After evaluating the phase diagram for the TIP4P model, Abascal and Vega proposed TIP4P/2005 [41]. This model retains the correct phase diagram, but the melting point is in better agreement with the experimental value. The bond geometry and the charge distribution in this model are the same as TIP4P except for the position of the M-site which is slightly shifted. The potential parameters of TIP4P/2005 were optimized to obtain a wide range of target properties. Along with the density of water at ambient conditions, the densities of solid phases were used to fit the parameters of this model. In addition, all target properties which were previously utilized in SPC/E and TIP5P models were used to optimize this model.

In addition to TIP4P-like models, SPC/E [39] is another popular water model. The charge distribution in this model is the same as TIP3P. The d_{OH} distance is 1 \AA and the angle between oxygen and two hydrogen atoms is 109.47°. Density and vaporization enthalpy were used to fit the parameters of this model. To reproduce the vaporization enthalpy, a polarization correction was incorporated into the model. SPC/E is a 3-site model and its computational cost is low making it very popular for large scale MD simulations.

Some properties of water predicted by the above models are shown in Table 1.2. The related experimental values are included for comparison. It can be seen from Table 1.2 that generally the 3-site models underestimate the melting temperature while TIP4P/2005 gives a closer value and TIP5P provides the best description of the melting point. Since

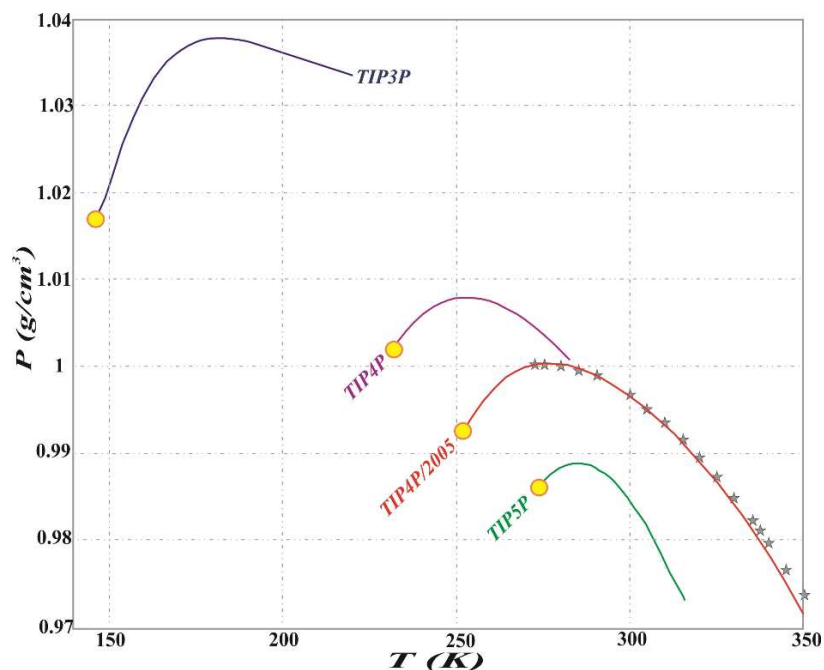


Figure 1.8: Dependence of density on temperature for the selected water models. Asterisks demonstrate experimental value. Squares represent the melting temperatures for each model. The graph is adapted from Ref [5].

the difference between the triple point temperature and the melting point for water is only about 0.01 K, the ratio between the melting point and the critical temperature (T_m/T_C) can demonstrate the range of existence of liquid water for different models [1,44]. According to the Table 1.2, the values for this ratio given by TIP4P models are closest to the experiment.

The temperature of maximum density (T_{MD}) for water is well reproduced by the TIP4P/2005 and the TIP5P models, although it should be noted that T_{MD} was one of the target properties used for optimizing these models. Figure 1.8 provides densities of water at various temperatures for the selected models. It can be seen that for temperatures at room pressure, it is the TIP4P/2005 model that reproduces the density of water.

The water molecule dipole moment for these models is higher than the experimental gas value in order to account for the polarization of the molecule in the liquid (see Table 1.2). In addition, it has been discussed in the literature that there should be a balance between the dipole and total quadrupole moments for the water model to provide a qualitatively reasonable description of the phase diagram [5,45]. It is obvious from Table 1.2 that

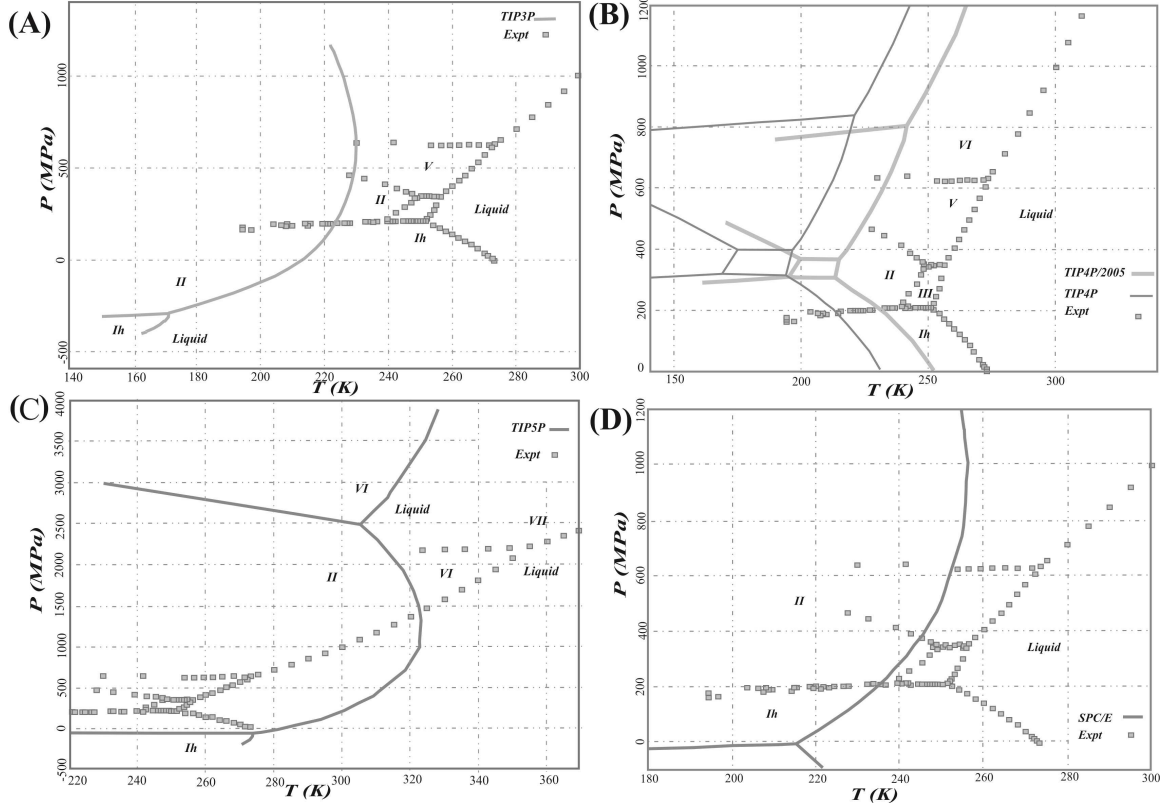


Figure 1.9: Phase diagram of the selected water models: (A) TIP3P, (B) TIP4P and TIP4P/2005, (C) TIP5P, and (D) SPC/E. Experimental symbols are shown for comparison. Frames (A), (B) and (C) are adapted from Ref. [5] and figure (D) is adopted and modified from Ref. [6].

the ratio between the dipole and quadrupole moments is very close to one for TIP4P and TIP4P/2005 models, while the other water models do not achieve this balance.

TIP4P/2005 provides a good result for the self-diffusion coefficient for liquid water at 278 K. SPC/E returns a reasonable prediction but the performance of the other models is quite poor.

The phase diagram of water obtained from these water models are compared with real water in Figure 1.9. It is obvious from this figure that except for TIP4P and TIP4P/2005, the other water models fail in reproducing the experimental phase diagram of water qualitatively. This is consistent with the related discussion on the ratio between dipole and quadrupole moments of water provided above. For the TIP3P, TIP5P and SPC/E models, ice Ih is stable only at negative pressures and the stable solid at 1 bar is ice II. The de-

scription of the phase diagram provided by TIP4P and TIP4P/2005 are similar (the phase diagram of TIP4P/2005 is shifted approximately 20 K to higher temperature, i.e. closer to experimental values) but the lines are shifted to higher pressure and lower temperature relative to real water.

The difference in the performance of these models at describing the properties of water appears to rely mainly on two factors: the charge distribution and the variety of target properties chosen for optimization. In fact, the choice of charge distribution (i.e. whether the negative charge position is on the oxygen atom, on the bisector of the H-O-H angle, or on the positions of the electron lone pairs) changes the multipole moments of the molecule which affect various properties of the model such as the phase diagram. For the TIP5P model, locating the negative charge on the lone pair electron positions results in small quadrupole moment for the molecule and a value of T_m/T_C that is too high. Locating the negative charge on the oxygen atom (as for TIP3P) weakens the hydrogen bonds which results in a low melting temperature and high diffusion constant [1].

The choice of target properties of water for optimization also affects the performance of the models. For example, the main difference between the SPC/E and TIP3P water models is the way they were optimized to reproduce the enthalpy of vaporization. Considering the self-polarization correction in reproducing this property in SPC/E increases the performance for this water model. In fact, incorporating more target values in the optimization process generally improves the quality of models. The increased availability of computational resources in recent years has allowed more properties of water to be considered in obtaining parameters of models.

The TIP4P/2005 model builds upon the successful ideas of previous models. Its geometry and charge distribution are almost the same as the TIP4P model as the TIP4P charge distribution demonstrates reasonably good performance in describing water behavior. In addition, a wide selection of target properties was considered in developing the TIP4P/2005 model. The successful idea of modifying the target value of the vaporization enthalpy, as

was done in the SPC/E model, was utilized for TIP4P/2005. Also, reproducing the temperature of maximum density and the phase diagram of water were included in the design of TIP4P/2005. In general, the performance of the TIP4P/2005 model is the best among the set of water models discussed here. In summary, the TIP4P/2005 model is reasonably accurate in describing water behavior and its computational cost is low relative to other more complicated water models. Therefore, by analyzing the performance of different water models for various properties of water, I have determined that the TIP4P/2005 water model is a good choice for these simulations.

1.5 Literature review

Ice growth from the water vapor has been the subject of many experimental studies. Also, the behavior of the quasi – liquid – layer on the ice surface has been explored in many experimental and theoretical works. However, the discrepancies in the reported results are significant. In this section, the relevant important theoretical and experimental studies reported in the literature are reviewed.

1.5.1 Experimental studies

1.5.1.1 Ice growth from vapor

Various experimental studies have investigated the growth behavior of ice from vapor and its dependence on temperature and supersaturation at the surface [46, 47]. Ice growth is typically controlled by various processes including transport phenomena as well as attachment kinetics. Attachment kinetics account for how water molecules are arranged into the ice structure and are related to the ice growth velocity by [14, 47]

$$v(T, \sigma_{surf}) = \alpha(T, \sigma_{surf})v_{kin}(T)\sigma_{surf}, \quad (1.25)$$

where $v(T, \sigma_{surf})$ is the growth velocity of ice, α is the dimensionless attachment coefficient (also known as the condensation coefficient), v_{kin} is the kinetic velocity, and σ_{surf} is the supersaturation above the ice surface.

Lamb and Scott [48] investigated the ice growth on a substrate at different temperatures and super saturations. According to their results, the dependence of the growth rates of the basal and prism faces on temperature demonstrates a local maximum for each. The temperature at which the maximum growth occurs at the prism face is shifted relative to the maximum growth on the basal face (-13°C and -6°C for the prism and the basal face, respectively). However, the measured ice crystals were large so the heating effects were not negligible. Also, as there were other crystals growing on the substrate that could act as vapor sinks and the super saturation may not have been accurate at points close to the observed crystals.

Sei and Gonda [49] studied the growth rates of basal and prism faces of ice as a function of supersaturation for a temperature range from -1°C to -30°C . The crystal was grown on a substrate in near-vacuum conditions. They found a repeated growth habit with decreasing temperature as plate (0°C to -4°C) \rightarrow column (-4°C to -10°C) \rightarrow plate (-10°C to -21°C) \rightarrow column (temperatures below -21°C). However, there is no discussion in this paper to clarify the substrate effect on the growth behavior.

In a more recent study, the reported morphological data provides the habit diagram of ice growth from vapor in air as a function of temperature [50]. Based on these data the ice crystals appear platelike (0°C to -4°C), columnar (-4°C to -8°C), again platelike (-8°C to -40°C) and columnar (-40°C to -70°C). These observations demonstrate that the growth rates are different for basal and prism faces at these temperature ranges.

Libbrecht [51] discussed the growth rates of the prism and basal facets of ice for temperatures ranging from -39°C to -10°C and proposed that the data can be described by a functional form

$$\alpha(\sigma) = Ae^{\left(\frac{-\sigma_0}{\sigma}\right)}. \quad (1.26)$$

In this model, $\alpha(\sigma)$ is the attachment coefficient, σ is the supersaturation, and $A(T)$ and $\sigma_0(T)$ are the measured functions. It was found in this paper that while there is no significant difference in σ_0 between both ice faces over this temperature range, $A(t)$ showed a minimum at $T = -15^\circ\text{C}$ for the basal face which shows a slow growth on this facet at that temperature. The author argues that this change is related to the surface melting transition for the basal face which is reported to be at about this temperature.

It has been discussed in the literature [46] that the discrepancies in the reported data of ice growth behavior from water vapor originate in the systematic effects that can perturb the measurements. These systematic errors include diffusion effects, substrate interactions and latent heat effects. Libbrecht and Rickerby [14] have presented more recent measurements of crystal growth on the principal facets of ice over a broader range of temperature (-2°C to -40°C) that attempt to minimize these systematic errors. The attachment kinetics follow the model proposed in previous work [47, 51] (Eq. 1.25). It has been shown by Libbrecht and Rickerby [14] that while the growth rate measurements on the basal face for all temperatures and on the prism face for temperatures below -10°C can be described with $A = 1$, for $T > -10^\circ\text{C}$ the growth data for prism face required $A < 1$. Also, for $T > -5^\circ\text{C}$, it was found that $\sigma_{0,basal} \gg \sigma_{0,prism}$ indicating the crystal growth on the prism face of ice is apparently much faster than on the basal surface in this temperature region.

The presence of significant discrepancies in the reported values for the growth rates on basal and prism faces of ice, which apparently arise mainly due to the measurement errors mentioned above, makes quantitative analysis difficult. However, it is generally acknowledged that the rates of crystal growth on the primary faces are different. In general, while the growth velocity on the prism face is higher at $T > -5^\circ\text{C}$ and $-20^\circ\text{C} < T < -10^\circ\text{C}$, the rate is faster on the basal face for $-10^\circ\text{C} < T < -5^\circ\text{C}$.

1.5.1.2 Quasi-liquid layer on the ice surface

Surface premelting occurs as a thin liquid-like layer of water forms on the ice surface without receiving heat from other surfaces at a given pressure and temperature just below its melting point [52]. Although the existence of surface premelting was first suggested by Faraday in 1842, the first measurements of the quasi-liquid layer (QLL) on the ice surface were in the 1980s [53]. Since then several techniques have been employed to measure the thickness of the QLL [52, 54]. All of these studies acknowledge the existence of a QLL on the ice surface near the melting point. Also, they confirm that the QLL thickness increases very fast with increasing temperature. But according to experimental reports, the observable premelting starts at -30°C [52]. However, the discrepancy in the reported experimental measurements of the dependence of the QLL thickness on temperature makes the comparison between them difficult [54]. There are several reasons for this variation. Various experimental techniques rely on various physical properties to determine the QLL thickness and so their results are different [52]. Doppenschmidt and Butt reported the thickness of the QLL as 11 nm at -10°C using atomic force microscopy [55]. Using photoelectron spectroscopy technique, Bluhm et al. measured the QLL thickness and its value at -10°C was reported as 5 Å [56]. More recently, Goertz and coworkers explored the QLL on the ice surface over the range -10°C to -30°C using interfacial force microscopy and the QLL thickness at -10°C was reported as 45 nm in this paper [57]. Another reason for the difference in the reported experimental data is the ice sample preparation procedure as some experiments are conducted on polycrystalline ice surfaces and some on thin ice films [52]. It is reported in the literature that the thickness of the QLL is different on the basal and prism faces of ice [58]. In addition, impurities in the experimental environment can change the thickness. Elbaum and coworkers reported that the QLL thickness increases with introducing a small amount of air to the surface of ice [59]. Also, Bluhm and coworkers demonstrated that hydrocarbon contamination can dramatically promote ice premelting [56].

In summary, it is acknowledged that by increasing the temperature below the melting point, the thickness of the QLL increases too. The uncertainties in the reported results are attributed to the use of different experimental techniques, the ice sample preparation procedure and the presence of impurities in the experimental procedure.

1.5.2 Theoretical studies

Due to the difficulties regarding the limits of the computational resources and an appropriate model to study ice growth behavior from water vapor using steady-state molecular dynamics simulations, there has been no simulation work in this field reported in the literature. However, the behavior of the quasi-liquid layer (QLL) formed on the surfaces of ice which is in contact with water vapor has been the subject of several different theoretical studies.

Fukazawa and Kawamura [60] studied the properties of the quasi-liquid layer on the basal surface of ice Ih. In this paper, the intensities of the peaks in the density profile corresponding to the first two layers of the ice structure are lower and broader than those of the other layers. Using the mean square displacement (MSD) of oxygen and hydrogen atoms, the authors showed that this phenomenon is due to the disordered arrangement and thermal vibrations of particles in these layers. These layers were labeled as surface layers of ice. It was argued in this paper that with an increase in temperature, the free O-H bond of surface molecules moves more freely and so the rotational motion of these molecules increases too. The increase in rotational motions distorts the surface ice lattice and the quasi-liquid layer forms in that region accordingly.

In another study, Conde and coworkers [7] explored the formation of the QLL on the basal, prism and secondary prism faces of ice Ih and its dependence on temperature for various water models (SPC/E, TIP4P, TIP4P/Ice and TIP4P/2005). The authors showed that the existence and thickness of the QLL do not depend on the water model when compared at the same undercooling relative to the melting point. For a given temperature, examining

the QLL thickness at different ice faces showed that its largest value is for the basal face and its smallest value is for the secondary prism face. Moreover, the authors argued that QLL formation begins for the basal, prism and secondary prism faces at 100 K, 80 K and 70 K below the melting point, respectively, and its thickness increases with increasing temperature. This dependence of QLL thickness on temperature is in general agreement with experimental measurements [56].

Neshyba et al. [61] explored the sublimation and deposition processes on the basal face of ice Ih at 250 K, this temperature being $\sim 40^\circ\text{C}$ below the melting point of the water model used in this work. Using density profile data, the authors defined the QLL as the outermost bilayer of the ice slab. Also, almost all of the striking water vapor molecules (with a probability of $>99\%$) were retained by the quasi-liquid layer. By counting the sublimation events, the vapor pressure at the interface was calculated as 240 Pa which is significantly greater than the experimental vapor pressure of ice at this temperature (76 Pa) [62]. It was argued that this difference is due to the lack of polarization in the NE6 potential model (the six site model of water [63]) which was used in this work.

In a more recent study, Pfalzgraff and coworkers [64] investigated the properties of the QLL on different faces of ice Ih in contact with vapor at 250 K ($\sim 40^\circ\text{C}$ below the melting point of the selected water model). According to their results, the thickness of the QLL on the basal, prismatic, 28° pyramidal and 14° pyramidal faces of ice Ih at this temperature were 0.67, 0.61, 0.63, 0.84 nm, respectively. Also, the QLL on all faces consisted of two sublayers. The anisotropic diffusivities in ice faces were also examined in this paper. The in-plane motion was reported to be faster in the prism to prism direction in comparison to the trans-basal direction. The smallest and greatest in-plane diffusion lengths were found to be for the 28° pyramidal and prismatic faces, respectively.

In summary, it has been shown that distortion of the ice surface is attributed for the formation of the QLL. The thickness of the QLL increases with increase in temperature. Also, it is confirmed that the QLL thickness is different on different ice faces and it is larger

on the basal face as compared with the prism face.

Chapter 2

STUDIES OF ICE GROWTH FROM WATER VAPOR

As mentioned in Section 1.5.2, although there are several experimental investigations on ice growth from the vapor phase in addition to various reports on the behavior of the quasi-liquid-layer on the free surface of ice, there have been no simulations of ice growth from vapor and the effect of the QLL on this phenomenon reported in the literature. Consequently, the main objective of this work is to provide a demonstration of proof of principle for the proposed model and method to probe this system.

In this section, the results from steady-state molecular dynamics simulations for ice while growing from vapor are presented. The temperature dependence of the growth behavior and the thickness of the quasi-liquid layer which forms on the ice surface at temperatures close to the melting point are also investigated. In addition, the QLL behavior on the basal and prism faces of ice at the selected temperatures are compared. The dependence of the QLL thickness on the steady-state fluxes of water vapor molecules is also examined.

The structure of this chapter is as follows. In section 2.1, the details of the simulations, the methods used in this work and the description of the system preparation are provided. In Section 2.2.1 an overview of the approach used in this work is explained. In Section 2.2.2 the temperature dependence of the thickness of the quasi liquid layer on the basal and prism faces of ice will be discussed. The surface behavior of the principle facets of ice are compared in Section 2.2.3. Finally, the dependence on the flux of particles is discussed in section 2.2.4.

2.1 Methodology

2.1.1 Simulation details

Since molecules are considered as rigid bodies in these simulations, their motions can be described in terms of the rotational motion about their centers of mass and the translational

motion of the centers of mass. In this work, the integration method for the translational molecular motions was the velocity Verlet algorithm [65, 66]. The rotational motions were integrated using a method that was introduced and used in previous work in the Kusalik group [67]. This method is based on the rotational velocity Verlet algorithm [68]. The time step for the integration of the equations of motion in all simulations was 2 fs.

All of the simulations in this work have been performed using classical rigid-body molecular dynamics. For describing the intermolecular interactions between water molecules the TIP4P/2005 water model was utilized. As the melting point of ice for this model is reported as 250.5 K [41], three different temperatures of 220 K, 235 K and 245 K have been chosen for this study. This range of undercooling was chosen in order to investigate the effect of temperature on the growth rate near the atmospheric melting point. Also, the growth behavior of ice from vapor was investigated on both basal and prism faces of hexagonal ice. An orthorhombic simulation box with periodic boundary conditions applied in all directions was used in all simulations. There were two phases in the periodic systems, where ice slabs were separated along the Z-direction by a gas phase. The length of all systems along the Z axis was approximately 150 Å and the X and Y dimensions of the simulation boxes of the basal and prism faces were $27 \times 31 \text{ Å}^2$ and $29 \times 32 \text{ Å}^2$, respectively. The basal and prism face systems contained 2208 and 2464 water molecules, respectively.

The cut off for the short-range Lennard-Jones interactions was chosen as 10 Å. The electrostatic interactions were described by the smooth particle mesh method of Ewald summation (SPME) [24]. During the preparation stage, the pressure was kept constant at 1 bar using a Berendsen barostat [27]. All production simulations were performed in the NVT ensemble and the target temperatures were maintained using a Nosé-Hoover chain thermostat [25] for each molecule (see Section 1.3.1). The simulations were carried out with the MDIce code which is an in-house classical molecular dynamics code developed and used in the Kusalik group [67].

All of the simulation runs in this work were carried out on the Simplex cluster which

is located in the Chemistry department of the University of Calgary. Each simulation was run on 4 cores in parallel with a wall-time of 100 – 300 hours.

2.1.2 System preparation

The initial ice crystal was generated [67] by placing the oxygen atoms on the lattice points given by the crystallographic parameters of hexagonal ice. The hydrogen atoms were assigned to the oxygen atoms according to the ice rules [3]. Then, the orientations of the water molecules were adjusted to minimize the total dipole moment of the ice in the simulation box while the ice rules were satisfied.

In order to generate a vapor phase, the ice crystal was divided into two equal slabs and each slab was displaced so that a gap was generated in the simulation box. The temperature of the systems was then increased starting from 0 K to the target temperature in a stepwise process. The difference in the temperature of each step was 50 K and in each step the system was equilibrated for 50 ps at 1 bar using the NPT ensemble. After reaching the target temperature, the system was also equilibrated for at least 2 ns using the NVT ensemble. When the steady – state was established (this was confirmed by observing the dynamics of the ice growth and the flux of particles), data have been collected and averaged for at least 50 ns. The equilibrated system for one of the simulations is shown in Figure 2.1. In this snapshot, the Z axis is perpendicular to the basal face. The typical time of production simulations was 50 ns, but data was collected from longer simulations for some systems when necessary. Data were sampled every 10 fs and the averages were saved every 1 ps (except for the root mean square (RMSD) values which have been saved every 10 ps) for post analysis.

2.1.3 Temperature profile and surface detection

In order to have ice growth on the surface of one ice slab, there should be a steady-state flux of water molecules moving toward it. In this study, to produce and control this flux, a



Figure 2.1: Snapshot from the configuration of the equilibrated system taken from the basal simulation at 245 K. Hydrogen and oxygen atoms are represented in white and red colors, respectively.

temperature pulse is introduced at the other side of the ice slab. The temperature pulse was generated by elevating the temperature in a specific region close to the evaporating surface and keeping the rest of the system at the target temperature which is below the melting point. The elevated temperature evaporates the water molecules and these molecules enter the gas phase moving toward the other surface where the ice grows at the target temperature. To have a consistent flux of separated water molecules and prevent cluster formation in the gas phase, and to provide a steady-state ice growth, the choice of appropriate parameters for this temperature pulse (such as location, width and height) was one of the main challenges. To obtain appropriate height and width for the temperature pulse, 10 simulations (with typical simulation time as 40 ns for each) were performed as test runs on the basal face at 245 K. Also, to ensure achieving the target temperature in the gas phase, the length of the gap between two ice slabs was chosen to be 50 Å along Z direction. In this work, the region of the elevated temperature was represented by a Gaussian-shaped temperature pulse with a broad peak at $T_M + 200$ K (to provide enough energy to evaporate the water molecules) introduced near the evaporating surface. I have tested many widths for the pulse (in the range of about 10 - 20 Å). In these simulations, it was found that a peak width of 17 Å at its half height worked well, where the center of the peak is located at a fixed distance from the position of the growing ice surface. This distance varies for different systems and must be chosen for each run. Displacement of the temperature pulse depends on crystal formation on the growing ice face in a way that the hot region moves into the ice

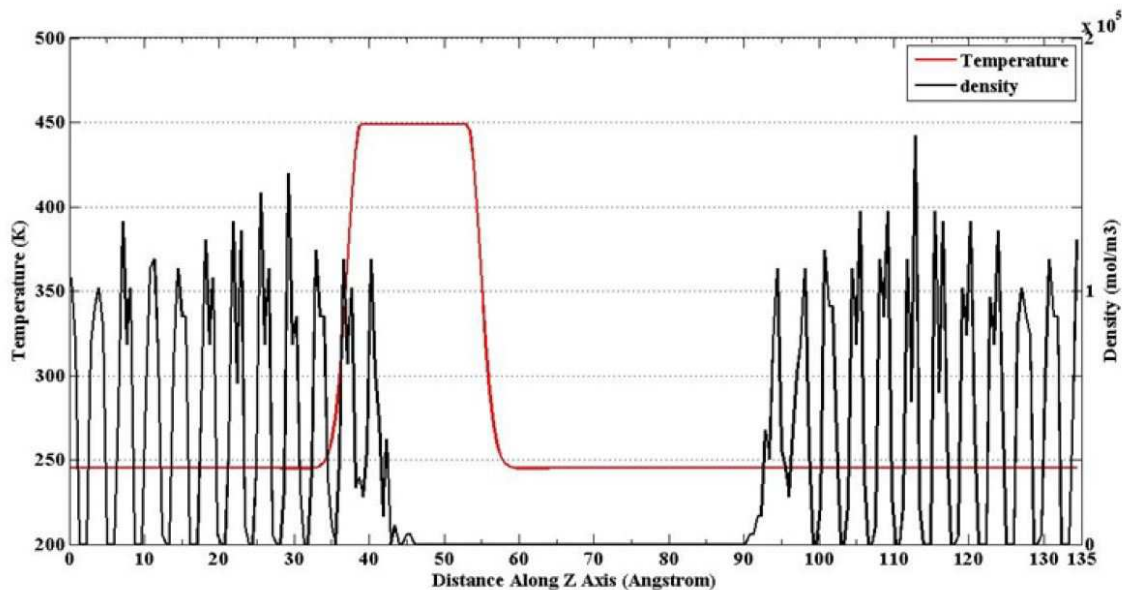


Figure 2.2: Density and temperature profiles for the initial state of the simulation on the basal face at 245 K.

during the simulation at the same rate as crystal grows. Figure 2.2 shows the initial density and the temperature profile for one of the simulations. In order to find the appropriate location of the temperature pulse relative to the melting ice interface, several test runs were performed on the basal and prism faces. On the basal face, 4, 8 and 5 simulations were performed at 220 K, 235 K and 245 K, respectively. On the prism face, 4 and 5 simulations were conducted at 220 K and 245 K, respectively. Also, for the prism face at 235 K, 14 simulations were carried out. Each of these test runs were performed for typically 50 ns. Steady-state ice growth was achieved on both faces at the selected temperatures with the relative distance between the temperature pulse and the melting ice interface in the range of about 14 - 20 Å.

When measuring the temperature profile in the systems from initial simulation runs, a discrepancy in the profile was observed between the gas and condensed phases. In the initial runs, it was the total temperature of a molecule that was controlled by the thermostat. While the target temperature was always achieved in the condensed phase, in the gas phase the translational temperature was consistently higher than the target value and the rotational

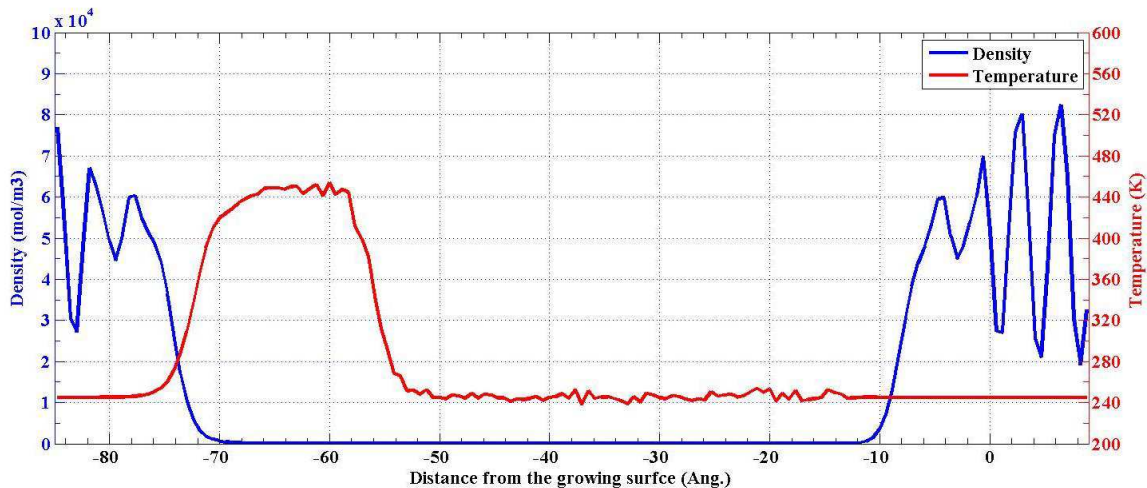


Figure 2.3: Comparison between the average density and temperature profiles for the simulation on the basal face at 245 K.

temperature was below it. In the condensed phase, water molecules are surrounded by other particles and their energies are constantly being exchanged, helping to ensure equi-partition of energy. This is not the case in the gas phase, where there is a lack of collisions and so no chance for the particles to exchange and redistribute their energies. With a single molecular thermostat, the heat bath interacts equally with rotational and translational degrees of freedom; consequently molecules will retain their initial temperature distributions. In this case, particles with higher translational kinetic energies are more successful at leaving the melting interface which gives rise to particles that are translationally hot and rotationally cold in the gas. To overcome this problem, I chose to control the translational and rotational temperatures separately. Figure 2.3 demonstrates a comparison between the average combined temperature and density profiles for one of the simulations. In this figure, it is evident that the target temperature is achieved across the simulation box.

The interface between two different phases can be determined from an inflection point on a property profile function that shows different behavior in the two phases [34]. In this work, the manifestation in the density profile of the ice crystal layering was used to find the position of the QLL-ice interface. The crystal structure is characterized by regularity in the positions of the molecules. This periodicity is detectable in the Fourier transformation of

the density profile [34]. The procedure used in the MDIce code to determine the QLL – ice interface is as follows [67]. Firstly, the density profile was evaluated on a grid of 256 points along the Z direction. For every grid point, Fourier transformation of the density profile was calculated for a fixed length window to the left ($\mathcal{F}_{left}(z)$) and right ($\mathcal{F}_{right}(z)$) side of each point. Then, by integrating over particular range of frequencies, the area under a specific peak (which corresponds to the ice interlayer distance) in the Fourier spectra, $\mathcal{F}_{left}(z)$ and $\mathcal{F}_{right}(z)$, were compared. When the difference between the areas of the two peaks for this particular frequency becomes maximized, the code evaluates the corresponding Z-grid point as the interface position.

Various property profiles have been examined in this study such as density, energy, temperature and mean squared displacement (MSD). Since crystal growth is a non-equilibrium process by nature, an averaged property profile over the simulation time should be obtained to study the growth behavior. In all simulations in this work, the averaging was done in the moving frame and not in the lab frame. The moving frame was attached to the growing ice surface and all averaged profiles have been calculated relative to the position of this interface. In all simulations, the box was divided into 256 bins along the z-axis and all property profiles were averaged over the simulation trajectory. The averaged energy and temperature profiles were calculated using the following formula:

$$\langle X \rangle_{\alpha} = \frac{\sum_{i=1}^N \langle X \rangle_{i,\alpha} \langle n \rangle_{i,\alpha}}{\sum_{i=1}^N \langle n \rangle_{i,\alpha}}, \quad (2.1)$$

where X is the quantity in each bin (such as energy), α is the number of each bin, N is the total number of time steps, $\langle n \rangle_{(i,\alpha)}$ is the number of water molecules in the bin.

2.2 Results and Discussion

2.2.1 Summary of the Results of Simulations

As one of the goals for this work was to study the dependence of the QLL thickness on temperature, it was necessary to have a criterion to distinguish the gas phase, solid phase and the QLL which forms in between. I should note that there is no unique method to map a molecular configuration into discrete phases and the results may vary depending on the choice of parameters and approach. Various property profiles of ice have been used in the literature to define the interface between the ice-like and the liquid-like regions of a system. The tetrahedral order of water molecules [7], average density profiles [7, 61, 64], and mean square displacement (MSD) of the atoms [60] have been used in different studies. Each of these parameters has its pros and cons which are described in the related works. As described in Section 2.1.3, using the previously developed method [67] that was available in the code, the Z-position of the interface between the QLL and ice was calculated in these simulations based on the periodicity of the density profile and was returned by the code at each simulation step. In the following, the approach to define the QLL layer and its thickness in these simulations will be described.

Figure 2.4 shows the average density and root mean square displacement (RMSD) profiles along the Z-axis for one of the simulations at 245 K. The time window to calculate the RMSD was 10 ps and the density data was sampled every 1 ps. It is evident that both profiles behave consistently. At the gas – QLL interface the profiles start to change at the same distance (about -14 \AA relative to the ice growing surface). Also, the RMSD is flat in the solid and it starts to rise as it goes into the QLL which is consistent with the average density behavior. The qualitative shape of the RMSD profile would stay the same independent of the choice of the length of the time window. However, in comparison with the density which is calculated from single particle properties, the RMSD is calculated over a time window and the values of the profile will change as the width of the time window changes.

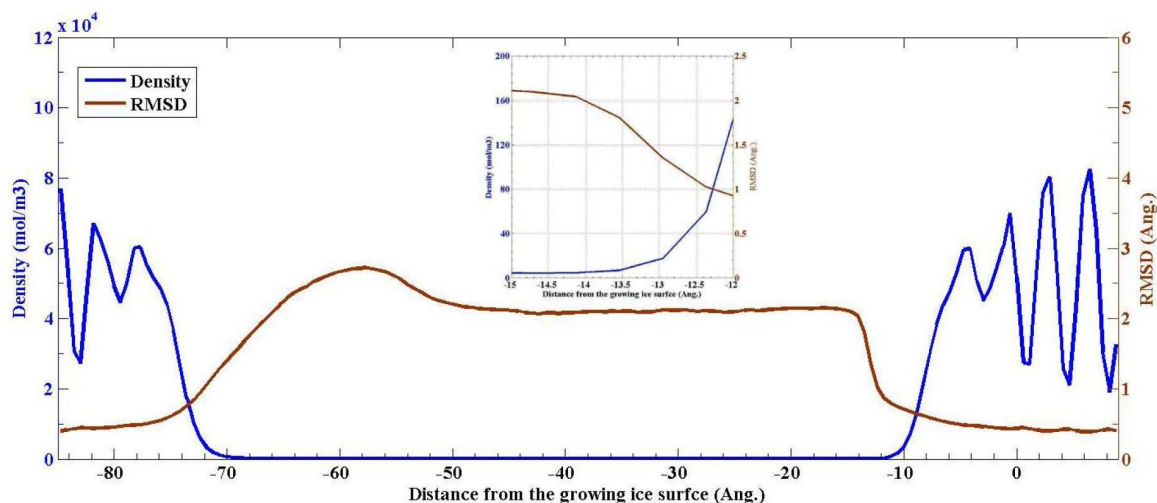


Figure 2.4: Average density and RMSD profiles along the Z-axis for one of the simulations on the basal face at 245 K. The inset graph shows the same comparison near the gas - QLL interface (-15 to -12 Å).

On the other hand, assuming sufficient sampling has taken place, the density profile should be independent of sampling frequency. Thus, I have chosen to utilize the density profile to determine the threshold between the gas phase and the QLL.

Figure 2.5 represents a comparison between the averaged density and the potential energy profiles at the interface for the same system. Again, both profiles show consistent behavior. The potential energy profile is almost flat in the solid phase and it starts to decrease in magnitude as it enters the QLL. Unlike the density which only depends on the number of particles in each bin, the potential energy depends on the interaction between pairs of particles. Consequently, the density can be unambiguously binned at particular Z distances in contrast with the potential energy which is not localized. Therefore, in comparison with the potential energy, the density profile is apparently a better choice for determining the position of the interface between the gas phase and the QLL.

Based on the arguments provided above, comparisons to the RMSD and the potential energy profiles, it was determined that the density profile is a better choice to determine the thickness of the QLL and how it might be impacted by different ice faces and temperatures. In order to identify the interface between the gas phase and the QLL, a

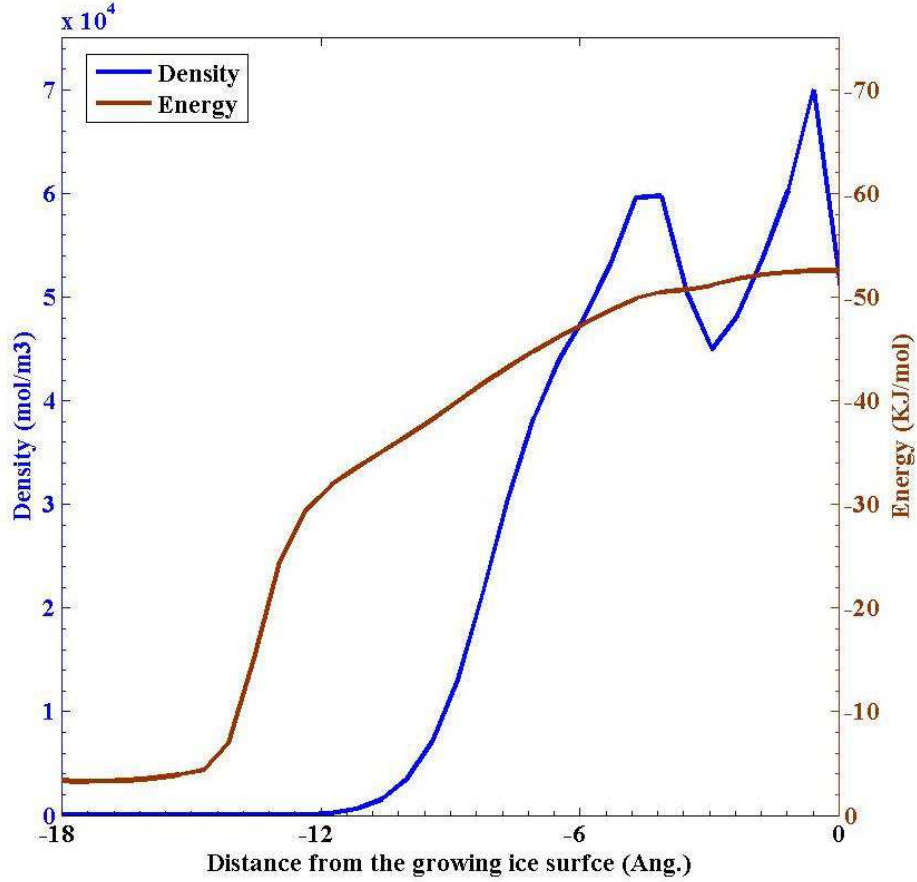


Figure 2.5: The averaged density and potential energy profiles at the interface for one of the simulations on the basal face at 245 K.

threshold was chosen based on the critical density of water for the TIP4P/2005 model; its value is $0.31 \frac{g}{cm^3}$ [41]. As the critical density is the highest density a gas phase can exist distinct from a liquid, it can reasonably provide a threshold value from which to argue the thickness of the QLL. I should point out that the critical temperature (640 K in TIP4P/2005 model [41]) is higher than any of the target temperatures in this work. Although the absolute value of the QLL thickness may depend on the choice of the threshold, as will be shown below the relative thicknesses of the QLL in this work are essentially independent of the specific choice of threshold.

Table 2.1 summarizes key parameters for the simulations performed in this work. The labeling convention of the simulations is based on the face of ice Ih on which the crystal growth was observed and the temperature at which the production simulation was carried

out. In the label, the first letter, b or *p*, corresponds to the basal or prism face, respectively, and the following number gives the system temperature. Also, at 245 K, I performed three simulations on the basal face with three different densities in the gas phase. the simulations with gas densities as 20, 9, and $6 \frac{\text{mol}}{\text{m}^3}$, are labeled as b245-1, b245-2 and b245-3, respectively. τ indicates the overall time of each simulation. During the simulations, the systems were monitored and for each system the distance between the temperature pulse and the evaporating surface was modified to achieve similar densities and prevent clusters forming in the gas phase. As these conditions were satisfied, and the final steady-state achieved, the averages for different property profiles (such as density, energy, temperature and positions of the evaporating and growing interfaces of ice) were collected for a minimum of 50 ns for post analysis. The distance between the center of the temperature pulse and the evaporating surface for all simulations was in the range of 3 – 5 Å.

There were some difficulties in obtaining steady state crystal growth from vapor as the MD code used for this work was originally designed to study the growth behavior of ice from the liquid water. As was mentioned in Section 2.1.3, the position of the temperature pulse is controlled by the instantaneous position of the growing ice surface. Therefore, any displacement of the growing surface causes the same for the pulse. For some simulations, particularly for systems with higher growth rate or greater surface fluctuations, this displacement was big enough to melt significant numbers of water molecules which typically resulted in cluster formation in the gas phase. As such events were undesirable, I usually had to change the position of the temperature pulse. It is recommended that for future work the methodology for determining the displacement of the temperature pulse during the simulation be modified. Specifically, instead of depending on the instantaneous position of the growing surface, the displacement of the temperature pulse would be calculated using a damping function.

The thickness of the ice grown during the simulations was used to find the growth rates given in Table 2.1. Figure 2.6 represents the time evolution of the growing ice surface

<i>Label</i>	<i>Face</i>	<i>Temperature</i>	ρ	σ	τ	R_{vapor}	R_{liquid}
		(K)	(mol/m ³)	(Å)	(ns)	(Å/ns)	(Å/ns)
<i>b220</i>	<i>Basal</i>	220	10	8.8	110	0.17	0.18
<i>b235</i>	<i>Basal</i>	235	30	9.1	110	0.52	0.60
<i>b245-1</i>	<i>Basal</i>	245	25	12.4	60	0.42	0.56
<i>b245-2</i>	<i>Basal</i>	245	9	9.8	90	0.13	0.56
<i>b245-3</i>	<i>Basal</i>	245	6	8.8	90	0.08	0.56
<i>p220</i>	<i>Prism</i>	220	20	7.6	90	0.33	0.34
<i>p235</i>	<i>Prism</i>	235	45	8.4	90	0.74	0.96
<i>p245</i>	<i>Prism</i>	245	25	10.2	60	0.45	0.87

Table 2.1: Summary of the key parameters and results for the simulations performed. ρ is the density in the gas phase, σ is the thickness of the quasi-liquid-layer, τ is the total simulation time, R_{vapor} is the measured growth rate from the vapor phase, and R_{liquid} is corresponding the growth rate from the liquid phase taken from [2]. Representative percentage errors for ρ , σ and R_{vapor} are 15%, 5% and 50% .

for the p220 simulation. It should be noted here that the slope of these curves does not return the actual growth rate as two factors contribute to the displacement of the growing interface; in addition to the new layers of ice, the ice slab experiences a net displacement to balance the net momentum asserted with the flux of molecules in the gas phase. Therefore, this extra displacement must be taken into account when finding the growth rate.

It is evident from Table 2.1 that on the same ice face, the growth is highest at 235 K which is about 15 K undercooling relative to the melting point of the water model. Also, at each selected temperature, the growth of ice is higher on the prism face. These results are in agreement with previous findings in the literature [14, 49, 50]. However, further investigation is required to verify these results, where determination of the rate of growth at more temperatures would be necessary to confirm if the ice growth from vapor has a dependence on temperature similar to the growth from the liquid.

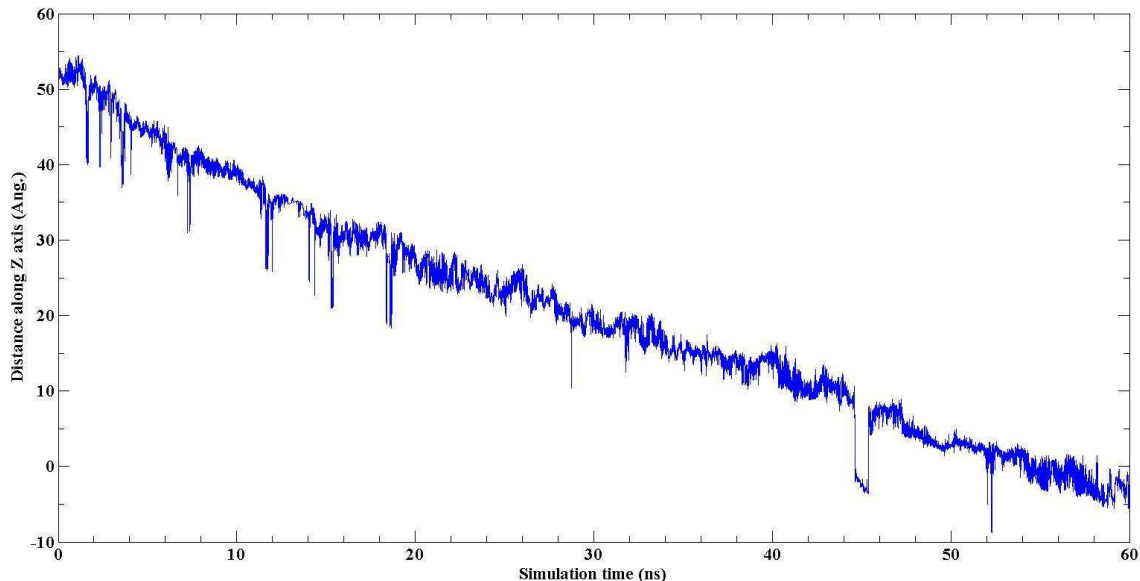


Figure 2.6: The time evolution of the position of the growing ice surface for the simulation on the prism face at 220 K. The positions are along the Z-axis in the lab frame.

2.2.2 Temperature dependence of the QLL thickness on different faces of ice

Experimental observations suggest that the QLL on the ice surface affects the growth mechanism [14]. It is also reported that the behavior of the QLL changes with temperature [7]. One of the outstanding questions regarding the behavior of ice growing from vapor is how the thickness of the QLL changes with temperature.

In order to study the dependence of the QLL thickness on temperature, I have conducted simulations to grow ice on the basal and prism faces at three temperatures: 220 K, 235 K and 245 K. The average density profiles at the selected temperatures for the growing basal and prism faces of ice are presented in Figures 2.7 and 2.8, respectively. In Figure 2.7, the density in the gas phase at the three temperatures is in the range 10 - 30 (mol/m^3). It is evident from this figure that, as the temperature increases, the thickness of QLL also increases. The QLL thickness values at 220 K, 235 K and 245 K are 8.8 Å, 9.1 Å, and 12.4 Å, respectively. In Figure 2.8 similar results from the growth on the prism face are presented. Again, with increasing temperature the thickness of the QLL increases where the thickness of the QLL on the prism face at 220 K, 235 K and 245 K are 7.6 Å, 8.4 Å

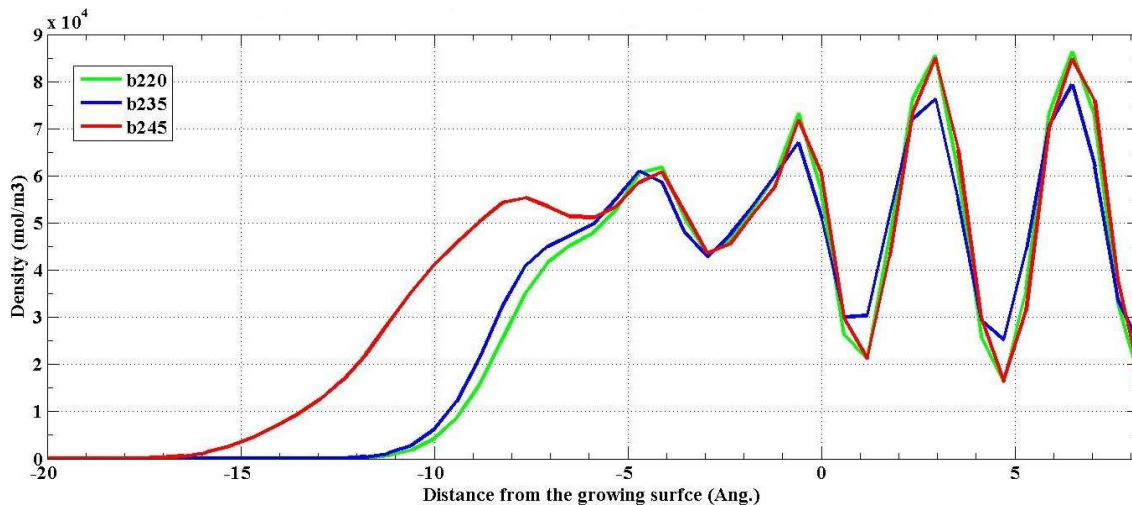


Figure 2.7: The average density profiles at the selected temperatures as a function of distance from the growing basal face of ice. The QLL thickness values for simulations at 220, 235, and 245 K are 8.8 Å, 9.1 Å, and 12.4 Å, respectively.

and 10.2 Å, respectively (see Table 2.1). The dependence of QLL thickness on temperature for basal and prism faces of ice observed here is in agreement with the work of Conde and coworkers [7]. Figure 2.9 compares the QLL thicknesses on the basal and prism faces with the corresponding values obtained by Conde et al. [7]. It should be noted that while in that work the thickness values have been measured at equilibrium conditions, the QLL thicknesses in this work were measured at steady-state ice growth. Also, different measurement method was used to identify the QLL thickness in the Conde et al. work, where the tetrahedral order parameter [69] was used to define the icelike and liquidlike molecules [7].

As shown in Figure 2.7, the increase in temperature does not change the behavior of the first two peaks of the QLL in the density profile for the basal face as all three curves are similar up to the distance of about - 6 Å. Although the thickness values increase with temperature, the distances between density profiles are relatively constant in QLL for distances beyond - 8 Å. According to Figures 2.7 and 2.8, at low temperatures, there are two layers of water molecules involved in the structure of the QLL on both faces. But as the temperature increases and gets closer to the melting point, one additional layer appears in the QLL density profile. In addition, this third peak appears broader. Fukazawa and

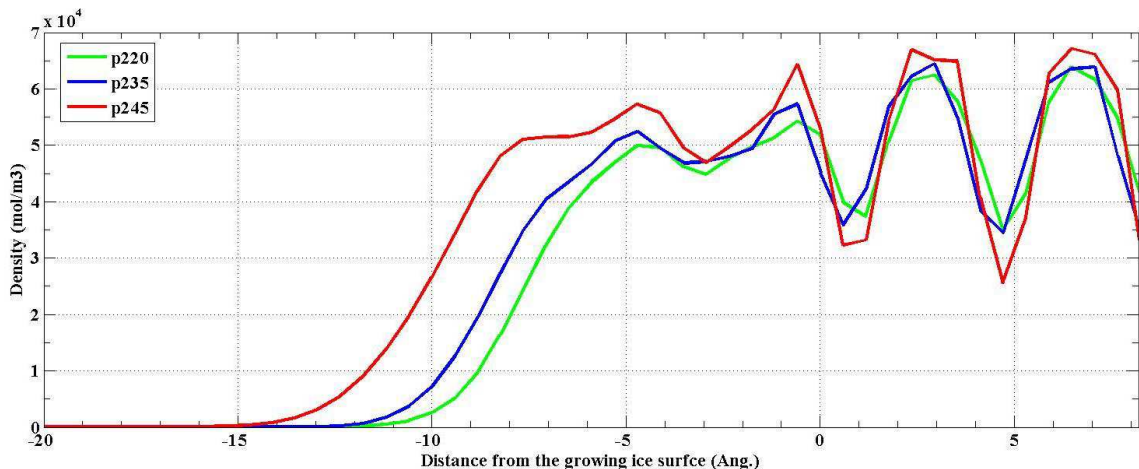


Figure 2.8: The average density profiles at the selected temperatures as a function of distance from the growing prism face of ice. The QLL thickness values for simulations at 220 and p245 K are 7.6 Å and 10.2 Å, respectively.

Kawamura [60] showed that this broadening is due to the disordered arrangement and the increased amplitude of the thermal fluctuations of the molecules in the QLL.

2.2.3 Comparison of the QLL thickness on the basal and prism faces of ice

As the structure of the basal and prism surfaces are different [3] this affects the characteristics of the QLL that forms on them. In Figure 2.10 the average density profiles for the basal and prism faces at 220 K are compared. Also, to provide further insight, instantaneous snapshots of configurations obtained for these facets at 220 K are presented in Figure 2.11.

As it can be seen in Figures 2.10, the quasi liquid layer which forms on the basal face is slightly thicker in comparison to the prism face (the QLL thickness for the b220 and p220 systems are 8.8 Å and 7.6 Å, respectively). Similar behavior is seen at 235 K and 245 K (see Table 2.1). This is consistent with the observation of Conde et al [7] who found that for ice Ih with a free surface that the basal QLL is thicker than the prismatic QLL.

In comparison with the prism face, the basal surface of ice is more rigid [3]. From Figures 2.10 and 2.11, it is evident that the QLL is more structured on the basal face relative to the prism face. This can be related to different structures of basal and prism surfaces.

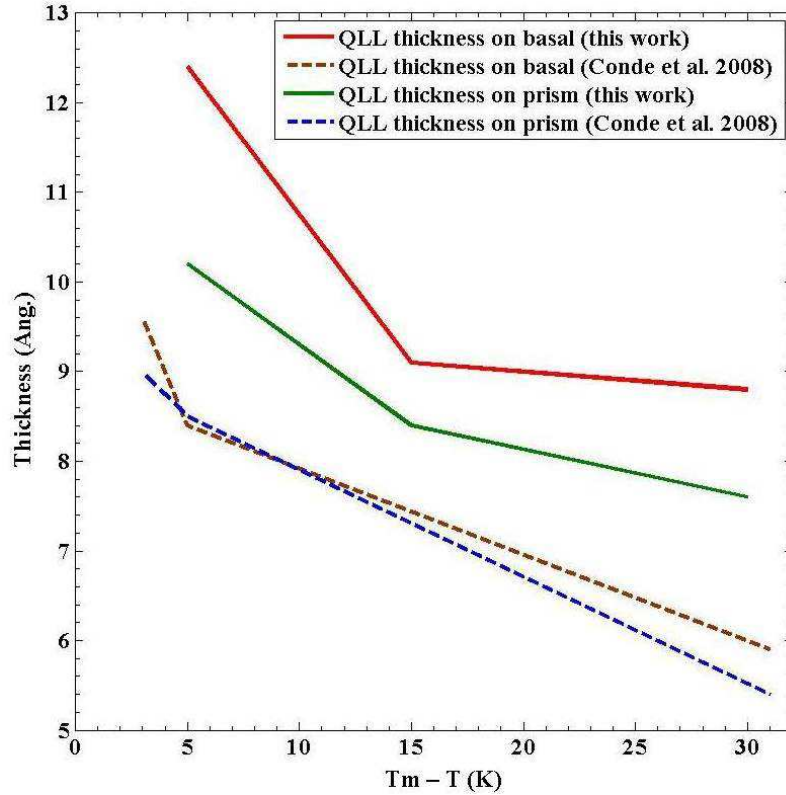


Figure 2.9: Results for the QLL thicknesses on the basal and prism faces obtained in this work in comparison with those obtained from ref. [7] as a function of the undercooling.

While a more structured QLL is attributed to the more structured basal surface, the rougher prism face results in a less structured QLL with broader density peaks.

2.2.4 Dependence of the QLL thickness on the flux of particles in gas

In the present simulations the rate of ice growth from vapor is controlled by the flux of particles in the gas phase which is directly related to the density of the gas. The water molecules which arrive at the surface become incorporated into the QLL which governs the growth behavior. Therefore, it would be of interest to examine how the flux of particles affects the QLL behavior.

The average density profiles taken from the MD simulations on the basal face of ice at 245 K with three different gas densities (b245-1, b245-2 and b245-3 simulations with gas densities of 25, 9, and 6 mol/m³, respectively) in the gas phase are presented in Figure 2.12.

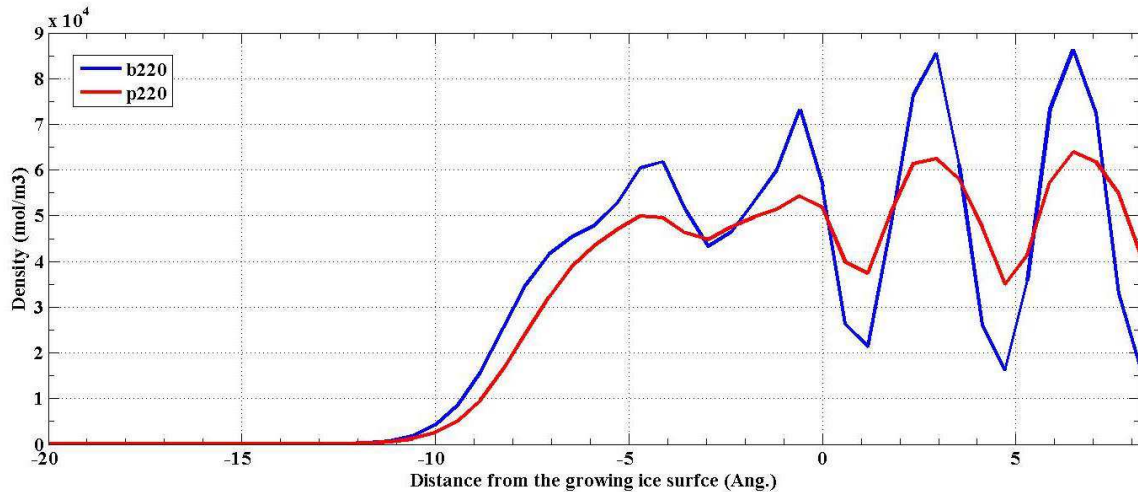


Figure 2.10: Comparison of the average density profiles for the basal and prism faces at 220 K.

In addition, the density profile for the b245-1 simulation is compared with the instantaneous configuration for the same simulation in Figure 2.13.

It is obvious from Figure 2.12 that by decreasing the flux of particles in the gas phase the thickness of the quasi liquid layer also decreases. The thickness of the QLL for b245-1, b245-2 and b245-3 are 12.4 Å, 9.8 Å, and 8.8 Å, respectively (see Table 2.1). Increasing the flux of particles in the gas appears to build up an extra layer on the QLL. The position of the peaks in the density profiles along the Z-axis remain constant for distances below - 8 Å.

One important question arises here: how does the flux of particles in the gas phase affect the growth rate of ice? In other words, how does the growth rate increase by increasing the gas density? While at low vapor pressure (or low gas densities) particle diffusion toward the interface plays more dominant role in controlling the growth mechanism and variation in vapor pressure changes the growth rate more significantly, at high gas densities, the thickness of the QLL increases and changes in vapor pressure have a smaller effect on the growth rate. In other words, at very high gas densities the QLL becomes similar to a liquid layer. Therefore, the growth rate from liquid water can be considered as an upper limit for the growth rate from vapor. The rates for growth from the liquid phase at the selected

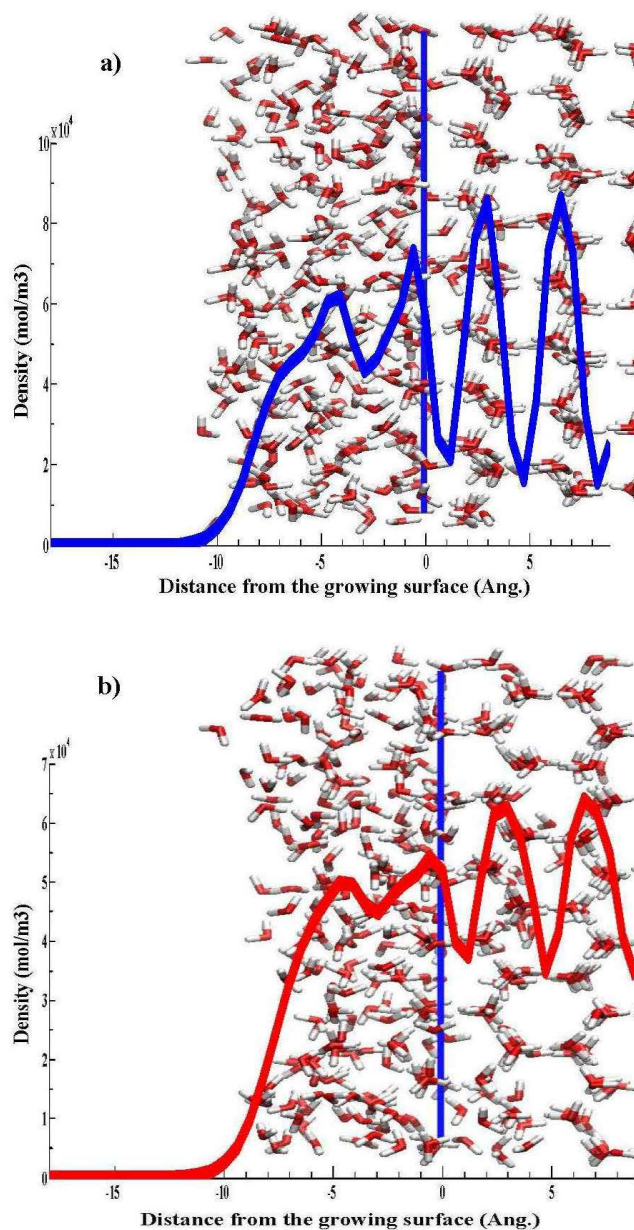


Figure 2.11: Average density profiles and instantaneous configurations obtained from the a) b220 and b) p220 simulations. The snapshots are taken normal to the direction of the growing ice surface. The vertical blue solid line represents the position of the ice surface determined by the MD code. Here, oxygen and hydrogen atoms are represented in red and white colors, respectively.

temperatures which are obtained from molecular simulations by Rozmanov and Kusalik [70] are provided in the Table 2.1 for comparison. All of the gas densities in this work are very high in comparison with the densities in experimental measurements (the vapor

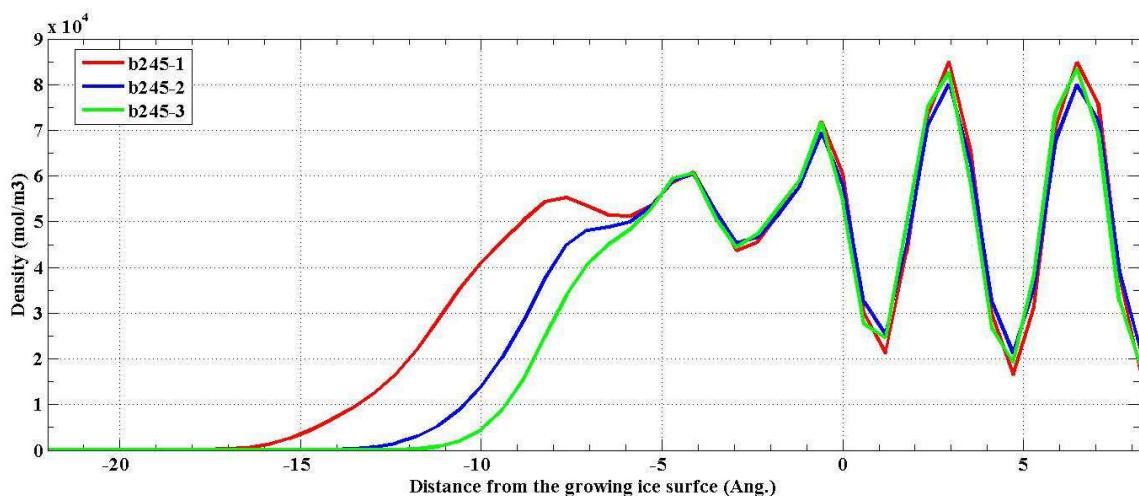


Figure 2.12: The average density profiles for the basal simulations at 245 K with densities in the gas phase of 20, 9, and 6 mol/m³, respectively. The QLL thicknesses for the b245-1, b245-2 and b245-3 systems are 12.4 Å, 9.8 Å, and 8.8 Å, respectively.

pressure at the ice surface is about two orders of magnitude lower in experimental studies, which is of the order of 10⁻³ bar [14, 71]) and the rate of growth is high and close to the corresponding values from the liquid phase. However, to estimate the crystal growth from lower gas densities using molecular simulations would be more computationally expensive. Longer simulation times are required to investigate the growth mechanism that is governed by gas diffusion.

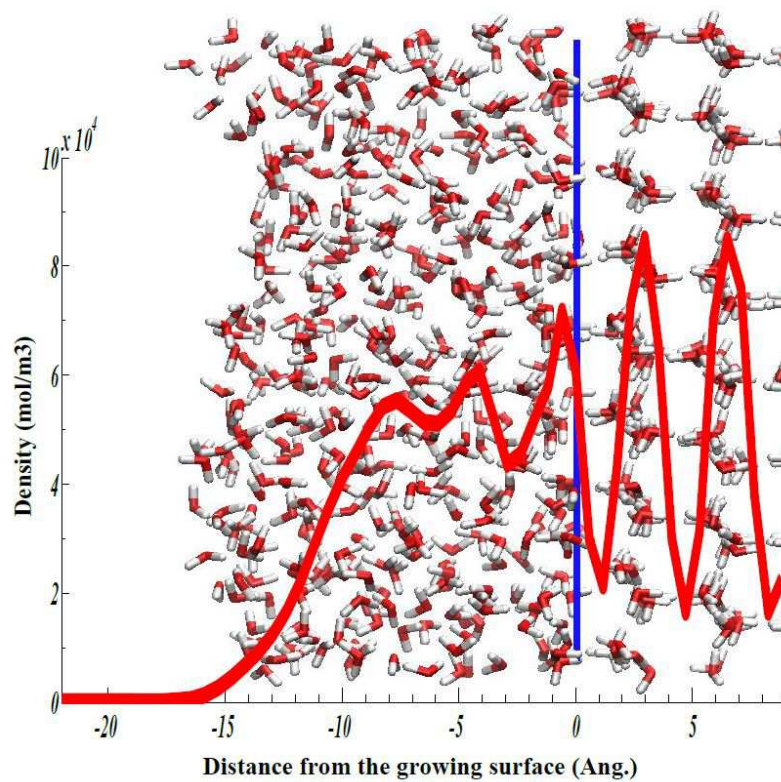


Figure 2.13: Comparison between the average density profile for the b245-1 system and an instantaneous configuration from the same simulation. The snapshot is taken normal to direction of the growing ice surface. The vertical blue solid line represents the interface Z coordinate calculated by the MD code. The oxygen and hydrogen atoms are represented in red and white colors, respectively.

Chapter 3

CONCLUSION AND FUTURE WORK

3.1 Conclusion

Due to the lack of an appropriate model, there have been no reports in the literature which explore the phenomenon of the ice growth from the water vapor from a microscopic point of view. Based on the methodology outlined in this thesis, molecular dynamics simulations were employed to maintain steady – state ice growth from the water vapor. The steady – state ice growth was achieved by introducing a temperature pulse near the evaporating ice surface. In this model, the displacement of the temperature pulse depends on crystal formation on the growing ice surface. Also, the dependence of the behavior of the quasi – liquid layer (QLL) that forms on the ice surface on temperature, ice face and flux of particles in the gas was investigated. The average density profile was utilized to analyze the behavior of the QLL.

Three different undercoolings of 5 K, 15 K and 30 K have been chosen for this study. It was found for all systems that with an increase in temperature the thickness of the QLL increases too. This dependence of QLL thickness on temperature for basal and prism faces of ice is consistent with that reported by Conde et al. [7].

In addition, the behavior of the QLL was investigated on growing basal and prism faces of hexagonal ice. It was shown that the QLL on the basal face is thicker than the prismatic QLL which is in agreement with the observation of Conde et al [7].

The rate of ice growth from water vapor is controlled by the density of particles in the gas phase as it is directly related to the particle diffusion. By choosing three different gas densities as 25, 9, and 6 mol/m³ the QLL behavior on the basal face at 245 K was monitored. Although increasing the flux of particles in the gas builds up an extra layer on the QLL, it did not change the shape and structure of sublayers in the QLL closer to the ice crystal.

This study provides groundwork for future atomistic investigations in the field of crystal growth from the vapor phase.

3.2 Future Work

Although for each selected temperature, the growth of ice was found to be faster on the prism face, which is consistent with the experimental measurements [49, 50, 72]; however it is not clear if this agreement was accidental. In order to obtain a better insight into the ice growth dependence on temperature, examining the rate of growth for a broader range of temperatures is suggested.

The MD code used for this work was originally designed to study the growth mechanism of ice from liquid water. In order to prevent cluster formation in the gas phase, it would be recommended for future work to modify the mechanism for determining the displacement of the temperature pulse during the simulation. So, instead of depending on the instantaneous position of the growing surface, the displacement of the temperature pulse over a time window can be calculated using a damping function.

All of the gas densities in this work were very large when compared with the densities in the experimental measurements and consequently, the rate of growth was large and close to the corresponding values from the liquid phase. In order to have a better understanding of the effect of particle diffusion on the growth mechanism, it would be advantageous to choose systems with a broader range of densities (including lower values) in the gas phase. However, this requires longer and consequently, more expensive simulations.

Bibliography

- [1] C. Vega and J. L. Abascal, “Simulating water with rigid non-polarizable models: a general perspective,” *Physical Chemistry Chemical Physics*, vol. 13, no. 44, pp. 19663–19688, 2011. (Cited on pages vii, 17, 20, 21 and 23.)
- [2] D. Rozmanov and P. G. Kusalik, “Temperature dependence of crystal growth of hexagonal ice (i h),” *Physical Chemistry Chemical Physics*, vol. 13, no. 34, pp. 15501–15511, 2011. (Cited on pages vii and 42.)
- [3] V. Petrenko and R. Whitworth, *Physics of Ice*. Clarendon Press, 1999. (Cited on pages viii, 2, 3, 4, 5, 6, 7, 33 and 45.)
- [4] C. G. Salzmann, P. G. Radaelli, E. Mayer, and J. L. Finney, “Ice xv: a new thermodynamically stable phase of ice,” *Physical review letters*, vol. 103, no. 10, p. 105701, 2009. (Cited on pages viii, 7 and 8.)
- [5] C. Vega, J. L. Abascal, M. Conde, and J. Aragones, “What ice can teach us about water interactions: a critical comparison of the performance of different water models,” *Faraday discussions*, vol. 141, pp. 251–276, 2009. (Cited on pages viii, 17, 18, 19, 20, 21 and 22.)
- [6] J. L. Abascal and C. Vega, “The water forcefield: Importance of dipolar and quadrupolar interactions,” *The Journal of Physical Chemistry C*, vol. 111, no. 43, pp. 15811–15822, 2007. (Cited on pages viii and 22.)
- [7] M. Conde, C. Vega, and A. Patrykiewicz, “The thickness of a liquid layer on the free surface of ice as obtained from computer simulation,” *The Journal of chemical physics*, vol. 129, no. 1, p. 014702, 2008. (Cited on pages ix, 8, 28, 38, 43, 44, 45, 46 and 51.)

- [8] P. V. Hobbs, *Ice physics*. Oxford University Press, 2010. (Cited on pages 1, 2, 3, 5 and 7.)
- [9] G. Petzold and J. M. Aguilera, “Ice morphology: fundamentals and technological applications in foods,” *Food Biophysics*, vol. 4, no. 4, pp. 378–396, 2009. (Cited on page 1.)
- [10] A. J. Baran, “A review of the light scattering properties of cirrus,” *Journal of Quantitative Spectroscopy and Radiative Transfer*, vol. 110, no. 14, pp. 1239–1260, 2009. (Cited on page 1.)
- [11] S. H. Faria, J. Freitag, and S. Kipfstuhl, “Polar ice structure and the integrity of ice-core paleoclimate records,” *Quaternary Science Reviews*, vol. 29, no. 1, pp. 338–351, 2010. (Cited on page 1.)
- [12] M. Allodi, R. Baragiola, G. Baratta, M. Barucci, G. Blake, P. Boduch, J. Brucato, C. Contreras, S. Cuyllé, D. Fulvio, *et al.*, “Complementary and emerging techniques for astrophysical ices processed in the laboratory,” *Space Science Reviews*, vol. 180, no. 1-4, pp. 101–175, 2013. (Cited on page 1.)
- [13] J. Dash, A. Rempel, and J. Wettlaufer, “The physics of premelted ice and its geophysical consequences,” *Reviews of modern physics*, vol. 78, no. 3, p. 695, 2006. (Cited on page 1.)
- [14] K. G. Libbrecht and M. E. Rickerby, “Measurements of surface attachment kinetics for faceted ice crystal growth,” *Journal of Crystal Growth*, vol. 377, pp. 1–8, 2013. (Cited on pages 1, 8, 24, 26, 42, 43 and 49.)
- [15] S. A. Clough, Y. Beers, G. P. Klein, and L. S. Rothman, “Dipole moment of water from stark measurements of h₂o, hdo, and d₂o,” *The Journal of Chemical Physics*, vol. 59, no. 5, pp. 2254–2259, 1973. (Cited on page 3.)

- [16] P. G. Debenedetti, “Supercooled and glassy water,” *Journal of Physics: Condensed Matter*, vol. 15, no. 45, p. R1669, 2003. (Cited on page 4.)
- [17] B. J. Murray, D. A. Knopf, and A. K. Bertram, “The formation of cubic ice under conditions relevant to earth’s atmosphere,” *Nature*, vol. 434, no. 7030, pp. 202–205, 2005. (Cited on page 7.)
- [18] C. G. Salzmann, P. G. Radaelli, B. Slater, and J. L. Finney, “The polymorphism of ice: five unresolved questions,” *Physical Chemistry Chemical Physics*, vol. 13, no. 41, pp. 18468–18480, 2011. (Cited on page 7.)
- [19] G. Tammann, “Ueber die grenzen des festen zustandes iv,” *Annalen der Physik*, vol. 307, no. 5, pp. 1–31, 1900. (Cited on page 7.)
- [20] P. W. Bridgman, “Water, in the liquid and five solid forms, under pressure,” in *Proceedings of the American Academy of Arts and Sciences*, pp. 441–558, JSTOR, 1912. (Cited on page 7.)
- [21] B. J. Gertner, J. T. Hynes, *et al.*, “Molecular dynamics simulation of hydrochloric acid ionization at the surface of stratospheric ice,” *SCIENCE-NEW YORK THEN WASHINGTON-*, pp. 1563–1565, 1996. (Cited on page 8.)
- [22] J. G. Calvert, I. U. of Pure, and A. Chemistry, *The chemistry of the atmosphere: its impact on global change*. Blackwell Scientific, 1994. (Cited on page 8.)
- [23] A. R. Leach, *Molecular modelling: principles and applications*. Pearson education, 2001. (Cited on pages 8, 9, 10, 11, 12, 13, 15 and 16.)
- [24] U. Essmann, L. Perera, M. L. Berkowitz, T. Darden, H. Lee, and L. G. Pedersen, “A smooth particle mesh ewald method,” *The Journal of chemical physics*, vol. 103, no. 19, pp. 8577–8593, 1995. (Cited on pages 12, 13 and 32.)

- [25] G. J. Martyna, M. L. Klein, and M. Tuckerman, “Nosé–hoover chains: the canonical ensemble via continuous dynamics,” *The Journal of chemical physics*, vol. 97, no. 4, pp. 2635–2643, 1992. (Cited on pages 13, 14, 15 and 32.)
- [26] S. Jang and G. A. Voth, “Simple reversible molecular dynamics algorithms for nosé–hoover chain dynamics,” *The Journal of chemical physics*, vol. 107, no. 22, pp. 9514–9526, 1997. (Cited on page 13.)
- [27] H. J. Berendsen, J. P. M. Postma, W. F. van Gunsteren, A. DiNola, and J. Haak, “Molecular dynamics with coupling to an external bath,” *The Journal of chemical physics*, vol. 81, no. 8, pp. 3684–3690, 1984. (Cited on pages 13, 15, 16 and 32.)
- [28] S. Nosé, “A unified formulation of the constant temperature molecular dynamics methods,” *The Journal of chemical physics*, vol. 81, no. 1, pp. 511–519, 1984. (Cited on page 13.)
- [29] W. G. Hoover, “Canonical dynamics: equilibrium phase-space distributions,” *Physical Review A*, vol. 31, no. 3, p. 1695, 1985. (Cited on pages 13, 14 and 15.)
- [30] S. Nosé, “A molecular dynamics method for simulations in the canonical ensemble,” *Molecular physics*, vol. 52, no. 2, pp. 255–268, 1984. (Cited on page 13.)
- [31] D. J. Evans and B. L. Holian, “The nose–hoover thermostat,” *The Journal of chemical physics*, vol. 83, no. 8, pp. 4069–4074, 1985. (Cited on page 13.)
- [32] D. Frenkel and B. Smit, *Understanding molecular simulation: from algorithms to applications*, vol. 1. Academic press, 2001. (Cited on page 13.)
- [33] S. Nosé, “A unified formulation of the constant temperature molecular dynamics methods,” *The Journal of chemical physics*, vol. 81, no. 1, pp. 511–519, 1984. (Cited on page 15.)

- [34] J. Vatamanu and P. Kusalik, “Molecular dynamics methodology to investigate steady-state heterogeneous crystal growth,” *The Journal of chemical physics*, vol. 126, no. 12, p. 124703, 2007. (Cited on pages 15, 36 and 37.)
- [35] T. A. Halgren and W. Damm, “Polarizable force fields,” *Current opinion in structural biology*, vol. 11, no. 2, pp. 236–242, 2001. (Cited on page 17.)
- [36] C. D. Wick, I.-F. W. Kuo, C. J. Mundy, and L. X. Dang, “The effect of polarizability for understanding the molecular structure of aqueous interfaces,” *Journal of Chemical Theory and Computation*, vol. 3, no. 6, pp. 2002–2010, 2007. (Cited on page 17.)
- [37] K. R. Hadley and C. McCabe, “Coarse-grained molecular models of water: a review,” *Molecular simulation*, vol. 38, no. 8-9, pp. 671–681, 2012. (Cited on page 17.)
- [38] W. L. Jorgensen, J. Chandrasekhar, J. D. Madura, R. W. Impey, and M. L. Klein, “Comparison of simple potential functions for simulating liquid water,” *The Journal of chemical physics*, vol. 79, no. 2, pp. 926–935, 1983. (Cited on page 19.)
- [39] H. Berendsen, J. Grigera, and T. Straatsma, “The missing term in effective pair potentials,” *Journal of Physical Chemistry*, vol. 91, no. 24, pp. 6269–6271, 1987. (Cited on pages 19 and 20.)
- [40] M. W. Mahoney and W. L. Jorgensen, “A five-site model for liquid water and the reproduction of the density anomaly by rigid, nonpolarizable potential functions,” *The Journal of Chemical Physics*, vol. 112, no. 20, pp. 8910–8922, 2000. (Cited on page 19.)
- [41] J. L. Abascal and C. Vega, “A general purpose model for the condensed phases of water: Tip4p/2005,” *The Journal of chemical physics*, vol. 123, no. 23, p. 234505, 2005. (Cited on pages 19, 20, 32 and 40.)

- [42] W. L. Jorgensen, J. Chandrasekhar, J. D. Madura, R. W. Impey, and M. L. Klein, “Comparison of simple potential functions for simulating liquid water,” *The Journal of chemical physics*, vol. 79, no. 2, pp. 926–935, 1983. (Cited on pages 18 and 19.)
- [43] C. Vega, E. Sanz, and J. Abascal, “The melting temperature of the most common models of water,” *Journal of Chemical Physics*, vol. 122, no. 11, pp. 114507–114507, 2005. (Cited on page 20.)
- [44] E. Paras, C. Vega, and P. Monson, “A generalized van der waals theory of solid-fluid equilibria for non-spherical molecules,” *Molecular Physics*, vol. 79, no. 5, pp. 1063–1072, 1993. (Cited on page 21.)
- [45] J. L. F. Abascal and C. Vega, “Dipole-quadrupole force ratios determine the ability of potential models to describe the phase diagram of water,” *Phys. Rev. Lett.*, vol. 98, p. 237801, Jun 2007. (Cited on page 21.)
- [46] K. G. Libbrecht, “A critical look at ice crystal growth data,” *arXiv preprint cond-mat/0411662*, 2004. (Cited on pages 24 and 26.)
- [47] K. G. Libbrecht, “The physics of snow crystals,” *Reports on progress in physics*, vol. 68, no. 4, p. 855, 2005. (Cited on pages 24 and 26.)
- [48] D. LAMB and W. SCOTT, “Linear growth rates of ice crystals grown from the vapor,” *COLLECTED REPRINTS-1972*, vol. 12, p. 203, 1972. (Cited on page 25.)
- [49] T. Sei and T. Gonda, “The growth mechanism and the habit change of ice crystals growing from the vapor phase,” *Journal of Crystal Growth*, vol. 94, no. 3, pp. 697–707, 1989. (Cited on pages 25, 42 and 52.)
- [50] M. P. Bailey and J. Hallett, “A comprehensive habit diagram for atmospheric ice crystals: Confirmation from the laboratory, air ii, and other field studies,” *Journal of the*

- Atmospheric Sciences*, vol. 66, no. 9, pp. 2888–2899, 2009. (Cited on pages 25, 42 and 52.)
- [51] K. Libbrecht, “Growth rates of the principal facets of ice between- 10° c and- 40° c,” *Journal of crystal growth*, vol. 247, no. 3, pp. 530–540, 2003. (Cited on pages 25 and 26.)
- [52] Y. Li and G. A. Somorjai, “Surface premelting of ice,” *The Journal of Physical Chemistry C*, vol. 111, no. 27, pp. 9631–9637, 2007. (Cited on page 27.)
- [53] A. Kouchi, Y. Furukawa, and T. Kuroda, “X-ray-diffraction pattern of quasi-liquid layer on ice crystal-surface,” *J. Phys.(Paris)*, vol. 48, pp. 675–677, 1987. (Cited on page 27.)
- [54] R. Rosenberg, “Why is ice slippery?,” *Physics Today*, vol. 58, no. 12, p. 50, 2005. (Cited on page 27.)
- [55] A. Döppenschmidt and H.-J. Butt, “Measuring the thickness of the liquid-like layer on ice surfaces with atomic force microscopy,” *Langmuir*, vol. 16, no. 16, pp. 6709–6714, 2000. (Cited on page 27.)
- [56] H. Bluhm, D. F. Ogletree, C. S. Fadley, Z. Hussain, and M. Salmeron, “The premelting of ice studied with photoelectron spectroscopy,” *Journal of Physics: Condensed Matter*, vol. 14, no. 8, p. L227, 2002. (Cited on pages 27 and 29.)
- [57] M. Goertz, X.-Y. Zhu, and J. Houston, “Exploring the liquid-like layer on the ice surface,” *Langmuir*, vol. 25, no. 12, pp. 6905–6908, 2009. (Cited on page 27.)
- [58] J. Dash, H. Fu, and J. Wettlaufer, “The premelting of ice and its environmental consequences,” *Reports on Progress in Physics*, vol. 58, no. 1, p. 115, 1995. (Cited on page 27.)

- [59] M. Elbaum, S. Lipson, and J. Dash, "Optical study of surface melting on ice," *Journal of crystal growth*, vol. 129, no. 3, pp. 491–505, 1993. (Cited on page 27.)
- [60] T. Ikeda-Fukazawa and K. Kawamura, "Molecular-dynamics studies of surface of ice ih," *The Journal of chemical physics*, vol. 120, no. 3, pp. 1395–1401, 2004. (Cited on pages 28, 38 and 45.)
- [61] S. Neshyba, E. Nugent, M. Roeselová, and P. Jungwirth, "Molecular dynamics study of ice- vapor interactions via the quasi-liquid layer," *The Journal of Physical Chemistry C*, vol. 113, no. 11, pp. 4597–4604, 2009. (Cited on pages 29 and 38.)
- [62] J. Marti and K. Mauersberger, "A survey and new measurements of ice vapor pressure at temperatures between 170 and 250k," *Geophysical Research Letters*, vol. 20, no. 5, pp. 363–366, 1993. (Cited on page 29.)
- [63] H. Nada and J. P. van der Eerden, "An intermolecular potential model for the simulation of ice and water near the melting point: A six-site model of h₂o," *The Journal of chemical physics*, vol. 118, no. 16, pp. 7401–7413, 2003. (Cited on page 29.)
- [64] W. Pfalzgraff, S. Neshyba, and M. Roeselova, "Comparative molecular dynamics study of vapor-exposed basal, prismatic, and pyramidal surfaces of ice," *The Journal of Physical Chemistry A*, vol. 115, no. 23, pp. 6184–6193, 2011. (Cited on pages 29 and 38.)
- [65] L. Verlet, "Computer" experiments" on classical fluids. i. thermodynamical properties of lennard-jones molecules," *Physical review*, vol. 159, no. 1, p. 98, 1967. (Cited on page 32.)
- [66] W. C. Swope, H. C. Andersen, P. H. Berens, and K. R. Wilson, "A computer simulation method for the calculation of equilibrium constants for the formation of physical clusters of molecules: Application to small water clusters," *The Journal of Chemical Physics*, vol. 76, no. 1, pp. 637–649, 1982. (Cited on page 32.)

- [67] D. Rozmanov, “Exploration of ice growth through molecular dynamics simulations,” 2012. (*Cited on pages 32, 33, 37 and 38.*)
- [68] D. Rozmanov and P. G. Kusalik, “Robust rotational-velocity-verlet integration methods,” *Physical Review E*, vol. 81, no. 5, p. 056706, 2010. (*Cited on page 32.*)
- [69] J. R. Errington and P. G. Debenedetti, “Relationship between structural order and the anomalies of liquid water,” *Nature*, vol. 409, no. 6818, pp. 318–321, 2001. (*Cited on page 44.*)
- [70] D. Rozmanov and P. G. Kusalik, “Anisotropy in the crystal growth of hexagonal ice, *ih*,” *The Journal of chemical physics*, vol. 137, no. 9, p. 094702, 2012. (*Cited on page 48.*)
- [71] T. Kuroda and R. Lacmann, “Growth kinetics of ice from the vapour phase and its growth forms,” *Journal of Crystal Growth*, vol. 56, no. 1, pp. 189–205, 1982. (*Cited on page 49.*)
- [72] K. G. Libbrecht and M. E. Rickerby, “Measurements of surface attachment kinetics for faceted ice crystal growth,” *Journal of Crystal Growth*, vol. 377, pp. 1–8, 2013. (*Cited on page 52.*)

Appendix A

SUPPLEMENTARY FIGURES

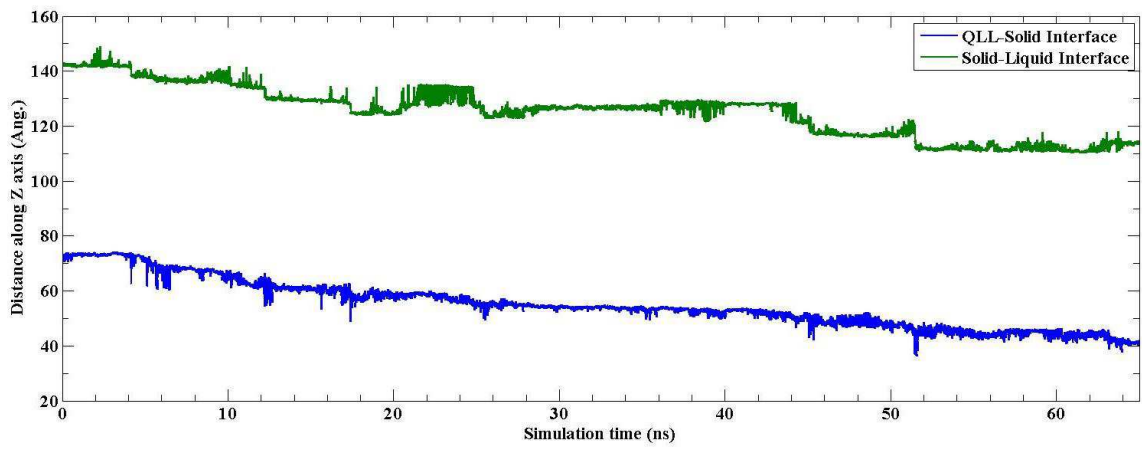


Figure A.1: The time evolution of the position of the surfaces for the simulation on the basal face at 220 K. The positions are along the Z-axis in the lab frame.

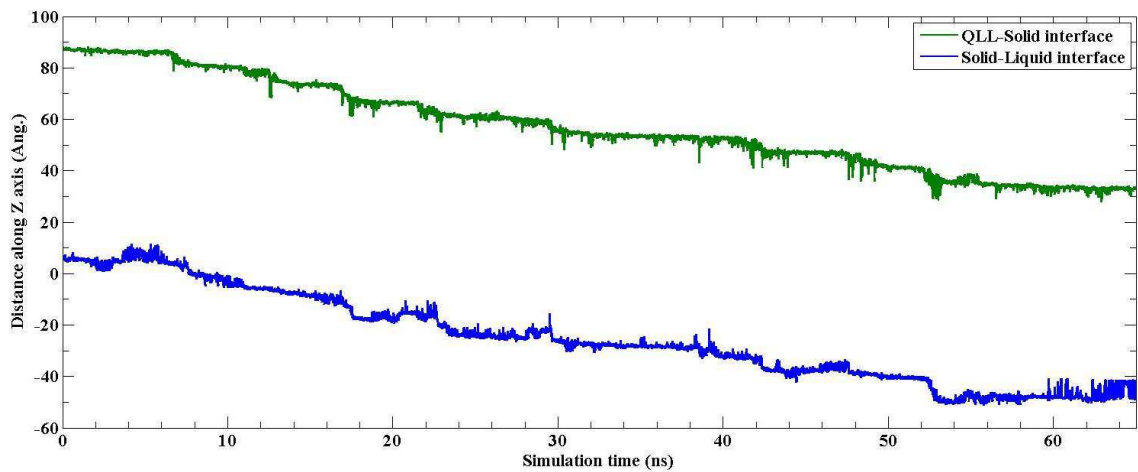


Figure A.2: The time evolution of the position of the surfaces for the simulation on the basal face at 235 K. The positions are along the Z-axis in the lab frame.

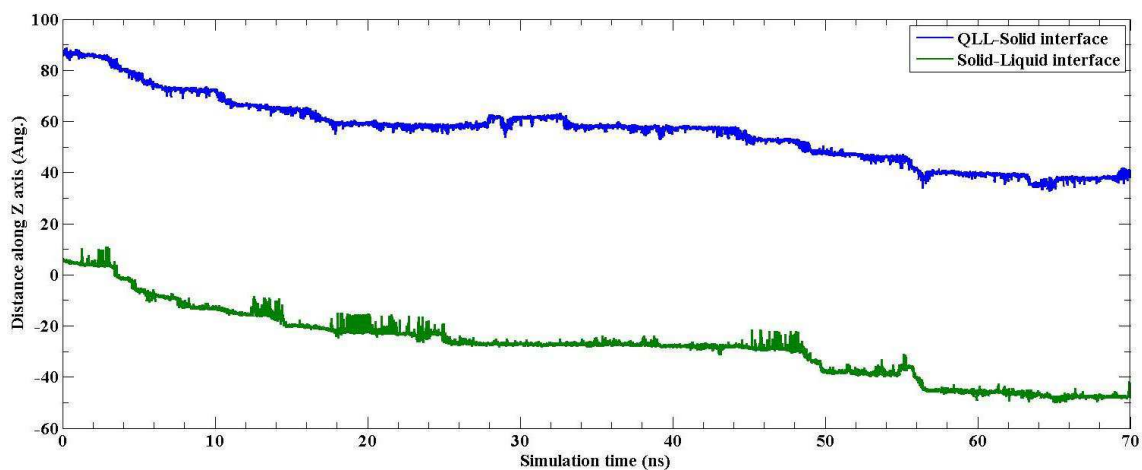


Figure A.3: The time evolution of the position of the surfaces for the simulation on the basal face at 245 K. The positions are along the Z-axis in the lab frame.

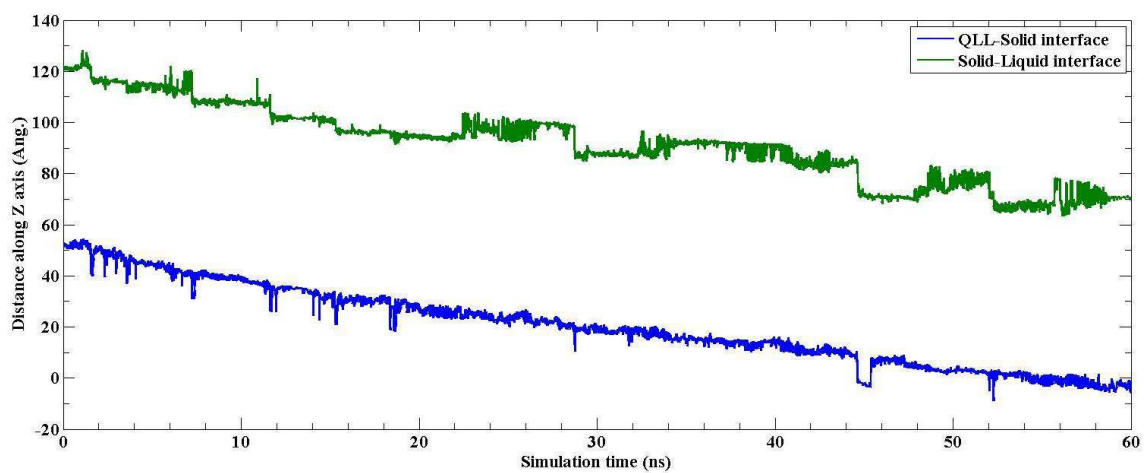


Figure A.4: The time evolution of the position of the surfaces for the simulation on the prism face at 220 K. The positions are along the Z-axis in the lab frame.

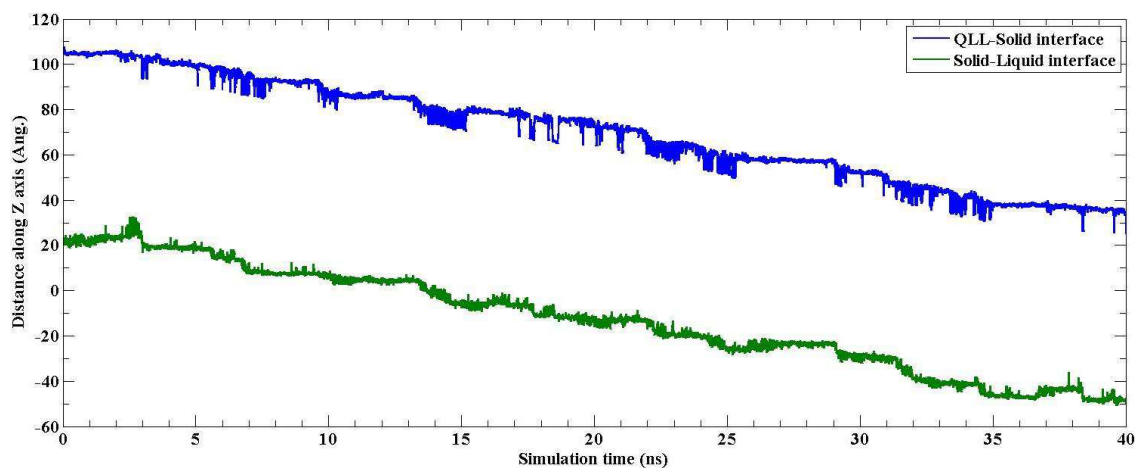


Figure A.5: The time evolution of the position of the surfaces for the simulation on the prism face at 235 K. The positions are along the Z-axis in the lab frame.

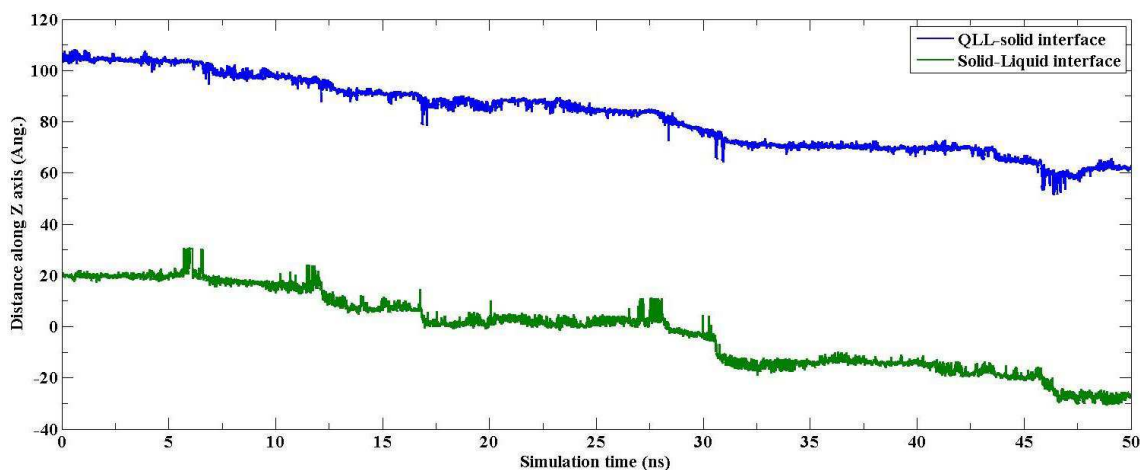


Figure A.6: The time evolution of the position of the surfaces for the simulation on the prism face at 245 K. The positions are along the Z-axis in the lab frame.

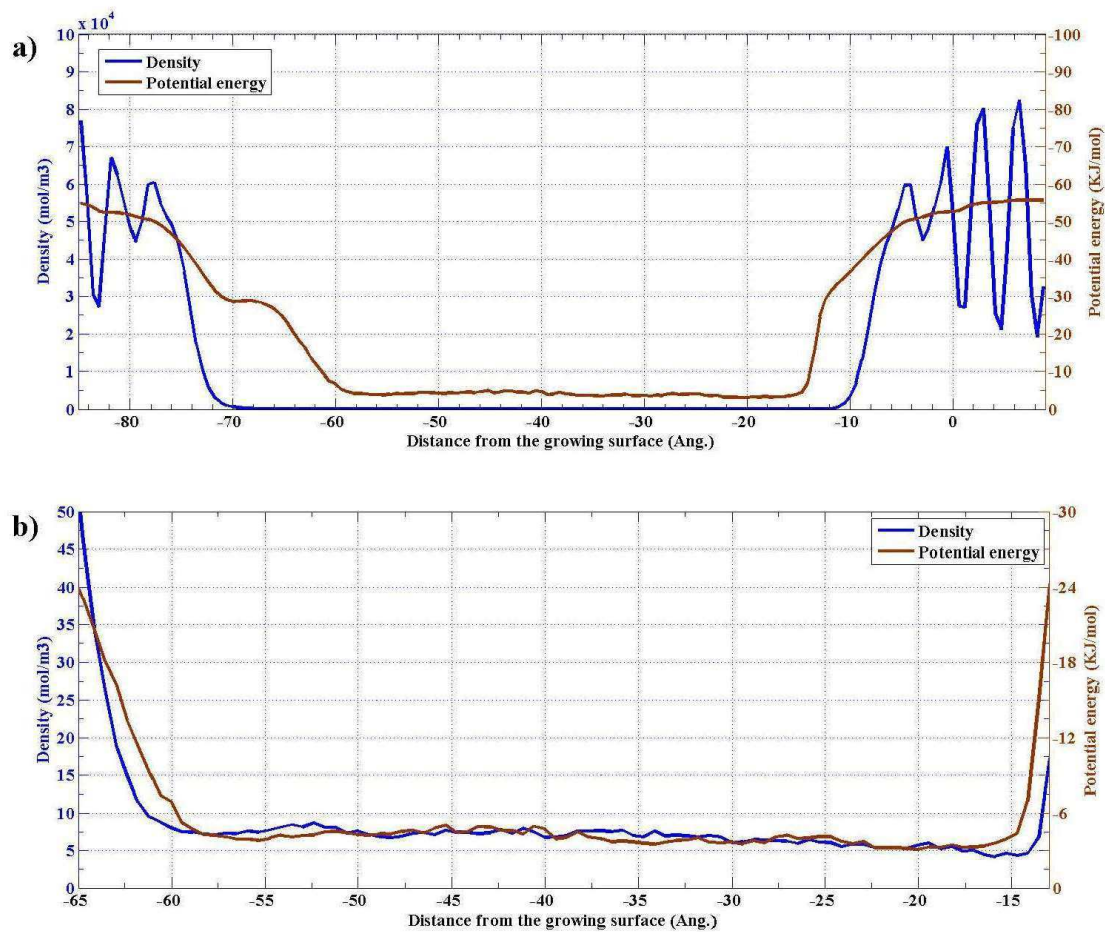


Figure A.7: the averaged density and potential energy profiles a) for the whole system and b) in the gas phase for one of the simulations on the basal face at 245 K.

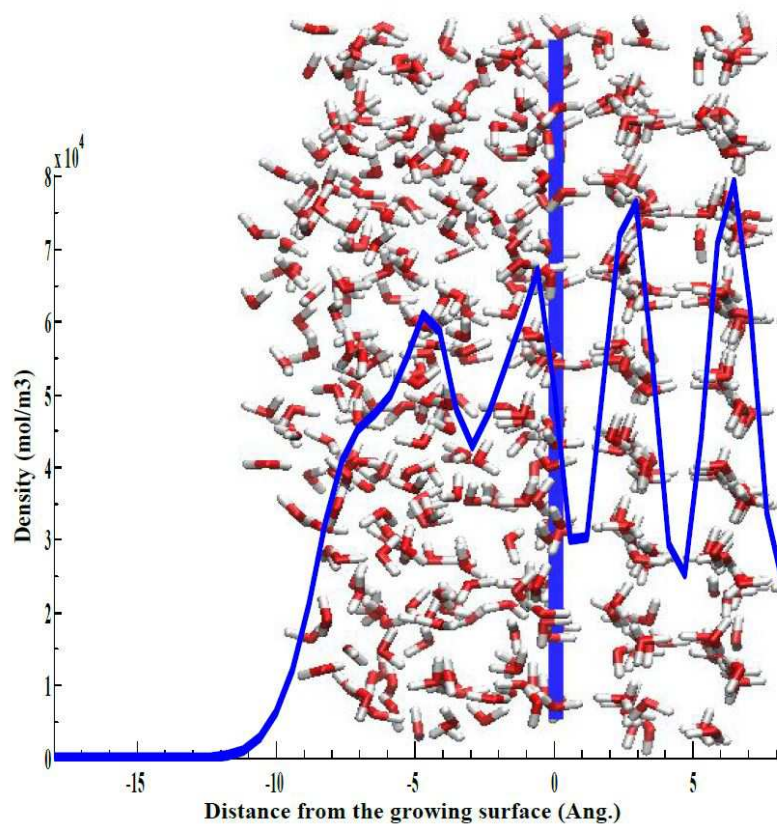


Figure A.8: Average density profiles and instantaneous configurations obtained from the b235 simulation. The snapshots are taken normal to the direction of the growing ice surface. The vertical blue solid line represents the position of the ice surface determined by the MD code. Here, oxygen and hydrogen atoms are represented in red and white colors, respectively.

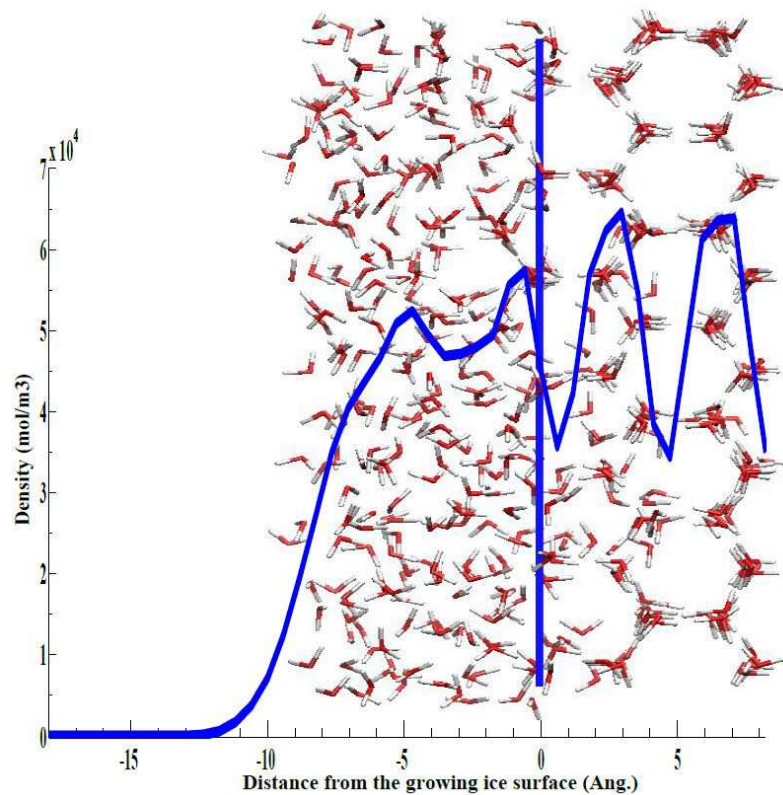


Figure A.9: Average density profiles and instantaneous configurations obtained from the p235 simulation. The snapshots are taken normal to the direction of the growing ice surface. The vertical blue solid line represents the position of the ice surface determined by the MD code. Here, oxygen and hydrogen atoms are represented in red and white colors, respectively.

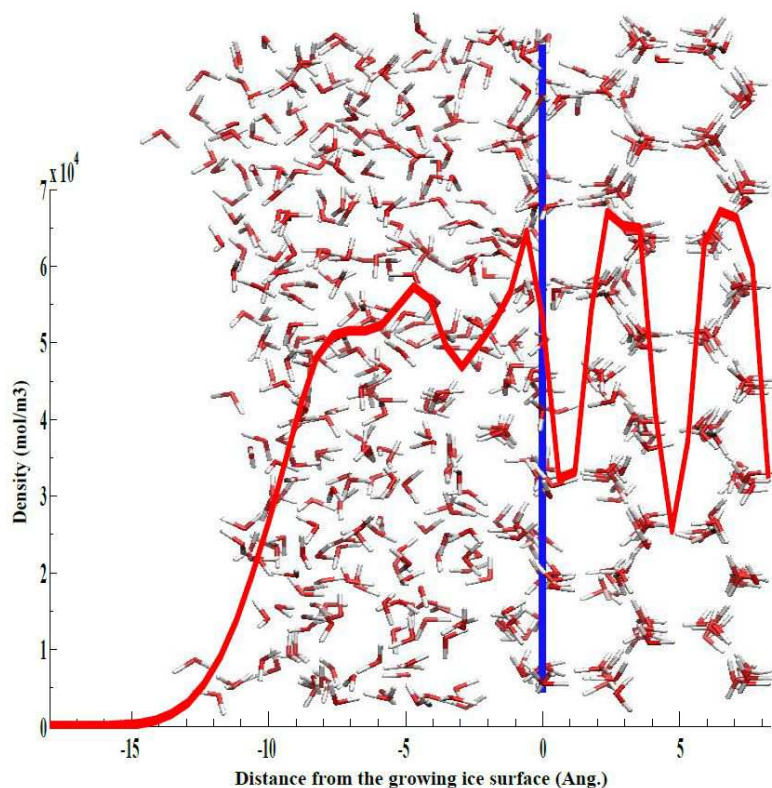


Figure A.10: Average density profiles and instantaneous configurations obtained from the p245 simulation. The snapshots are taken normal to the direction of the growing ice surface. The vertical blue solid line represents the position of the ice surface determined by the MD code. Here, oxygen and hydrogen atoms are represented in red and white colors, respectively.

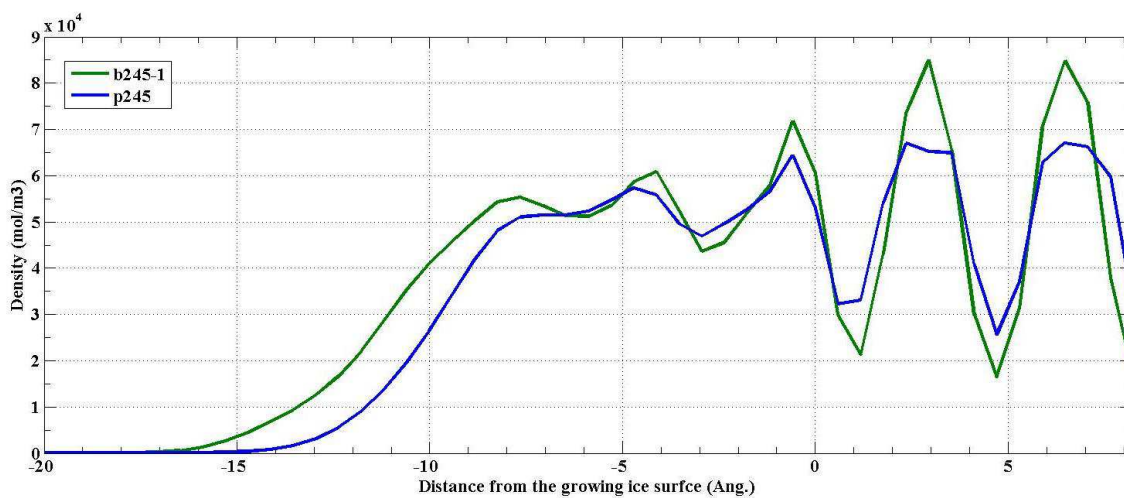


Figure A.11: Comparison of the average density profiles for the basal and prism faces at 245 K.